Lawrence Smith
EM11

COMPUTATIONAL FLUID DYNAMICS COMBUSTION ANALYSIS EVALUATION

Final Report

Contract No: NAS8-36955 D.O.116
Report Number CCFD-92-02

By

Y.M. Kim, H.M. Shang, C.P. Chen, and J.P. Ziebarth
University of Alabama in Huntsville, Huntsville, AL 35899

April, 1992

For
CFD Branch(ED32)
George C. Marshall Space Flight Center
National Aeronautics and Space Administration
Marshall Space Flight Center, Alabama 35812

ABSTRACT

This study involves the development of numerical modelling in dilute and dense spray combustion. We discuss several issues concerning the computational efficiency in the stochastic particle tracking method as well as the improvement of physical submodels of turbulence, combustion, vaporization, swirling effects, and dense spray effects. The governing gas-phase equations in Eulerian coordinate are solved by a time-marching multiple pressure correction procedure based on the operator-splitting technique. The droplet-phase equations in Lagrangian coordinate are solved by a stochastic discrete droplet technique. The $k-\epsilon$ model is used to characterize the time and length scales of the gas phase turbulence for droplet dispersions and droplet/turbulence interactions. To improve the computational efficiency in the stochastic tracking calculations, we implement a dispersion width transport model which can account for turbulent dispersion within each computational parcel. The testings of this model confirm the capability of accuratly representing dispersion in nearly-homogeneous and inhomogeneous turbulent flows with improved efficiency over the delta function stochastic separated flow(SSF) model. To account for the dense spray effects, we have employed an existing drop collision and coalescence model and a Taylor analogy breakup(TAB) model. These models were incorporated into a state-of-the-art multiphase all-speed transient flow solution procedure. A sequence of validation cases involving non-evaporating, evaporating, burning, dilute and dense spray cases are included. The research tasks concerning the development of multidimensional group particle tracking method and particle wall-boundary condition are separately documented in Appendix E.

TABLES OF CONTENTS

ABSTRACT

NOMENCLATURE

1. INTRODUCTION

    1.1 General

    1.2 Turbulent Particle Dispersion

    1.3 Dilute Spray Models

    1.4 Dense Spray Models

2. MATHEMATICAL MODELLING OF THE MULTI-PHASE FLOWS

    2.1 Basic Eulerian Equations

    2.1.1 Mean Flow Equations

    2.1.2 Turbulence Models

    2.1.3 Combustion Models

    2.2 Basic Lagrangian Equations

    2.2.1 Droplet-Phase Mass & Heat Transfer Equations

    2.2.2 Turbulence/Droplet Interaction Model

    2.2.3 Drop Breakup and Collision Model

    2.2.4 Droplet/Wall Impingement Model

3. NUMERICAL MODEL AND BOUNDRAY CONDITIONS

4. RESULTS AND DISCUSSIONS

    4.1 Turbulent Particle Dispersion

    4.1.1 Nearly-Homogeneous Turbulent Dispersion

    4.1.2 Inhomogeneous Turbulent Dispersion

    4.2 Dilute Spray Combusting Flows

    4.2.1 Hollow-Cone Kerosene Spray Flames

    4.2.2 Spray Flame with a Rotating-Cup Atomizer

    4.3 Dense Sprays

4.3.1 Non-Evaporating Solid-Cone Spray
4.3.2 Non-Evaporating Hollow-Cone Spray
4.3.3 Evaporating and Burning Sprays

5. CONCLUSIONS

6. RECOMMENDATIONS

APPENDIX

A. Two-Phase Interaction Source Terms

B. Numerics of Beta Probability Density Function

C. Stoichiometric Relations For Hydrocarbon Fuels

D. Droplet Distribution Models

E. Adaptation of Multidimensional Group Particle Tracking and Particle Wall-Boundary Condition Model To The FDNS Code (Contract Report from SECA, Inc.)

NOMENCLATURE

B_m : mass transfer number

B_t : heat transfer number

C_p : heat capacity of air

$C_{p,d}$: heat capacity of droplet

C_D : drag coefficent

d_p : droplet diameter

D : diffusion coefficient in Fick's law

E : mean specific internal energy

E_p : specific internal energy of particle

f : mixture fraction

Fp_i : particle drag force

g : gravity

h : enthalpy of gas phase

h_f : fuel vapor enthalpy

K : undersampling correction factor

k : turbulent kinetic energy

L : latent heat

N_t : number of droplets for each computational particle p

N_P : number of computational particles

P : probability

p : mean pressure

Pr_t : turbulent Prandtl number

Re_p : particle Reynold's number

r_p : droplet radius

u_i : instantaneous velocity for gases

v_i : instantaneos velocity for droplets

S : source terms

Sc_t : turbulent Schmidt number

T : gas temperature

t : time

T_d : droplet temperature

x : coordinate in the streamwise direction

Y : mass fraction

y : coordinate normal to the streamwise direction

Greek Symbol

ρ : density of gases

ρ_f : fuel vapor density

ρ_d : droplet density

μ : viscosity

μ_t : eddy viscosity

ϕ : instantaneous scalar for gases

ϵ : turbulent energy dissipation rate

ξ : instantaneous mixture fraction

τ : particle relaxation time

σ : standard deviation of pdf

σ^2 : variance of pdf

Subscripts

f : fuel

g : gas phase

i : time step index in an eddy

k : eddy index

l : liquid phase

p : particle or parcel

rms : root mean square

t : turbulent

Supercripts

$-$: density-averaged

$'$: fluctuating

NASA
National Aeronautical and Space Agency

Report Document Page

1. Report No.	2. Government Accession No.	3. Recipient's Catalog No.
11		

4. Titile and Subtitle
COMPUTATIONAL FLUID DYNAMICS COMBUSTION ANALYSIS EVALUATION

5. Report Due
April 10, 1992

6. Performing Organization Code
University of Alabama in Huntsville

7. Aurthor(s)
Y. M. Kim
H. M. Shang
C. P. Chen
J. P. Ziebarth

8. Performing Organization Report No.

10. Work Unit No.
D.O. 116 5-32638

9. Performing Organization Name and Address
University of Alabama in Huntsville
Huntsville, Alabama 35899

11. Contract or Grant No.
NAS8-36955, D.O. 116

12. Sponsoring Agency Name and Address
National Aeronautics and Space Administration
Washington, D.C. 20546-001
Marshall Space Flight Center, AL 35812

13. Type of report and Period covered
FINAL - 04/11/91 - 04/10/92

14. Sponsoring Agency Code

15. Supplementary Notes

16.Abstract

This study involves the development of numerical modelling in spray combustion. These modelling efforts are mainly motivated to improve the computational efficiency in the stochastic particle tracking method as well as to incorporate the physical submodels of turbulence, combustion, vaporization, and dense spray effects. The present mathematical formulation and numerical methodologies can be casted in any time-marching pressure correction methodologies (PCM) such as FDNS code and MAST code. A sequence of validation cases involving steady burning sprays and transient evaporating sprays will be included.

17. Key Words (Suggested by Author(s))	18. Distribution Statement
Spray Combustion, Fuel Evaporation, Swirling Flows, Droplet Dispersion, and Dense Spray Effects	Unclassified - Unlimited

19. Security Class. (of this report)	20. Security Class. (of this page)	21. No. of pages	22. Price
Unclassified	Unclassified	85	

NASA FORM 1626 OCT 86

omit

1. INTRODUCTION

1.1 General

There have been a number of research efforts[1-6] towards the development of numerical and physical models for spray combustion. Many aspects of sprays including fuel properties of droplets [1], multicomponent nature of fuel [2], evaporation models [3] have been studied and excellent reviews on analysis and measurements of sprays have also been given in Refs. [4,5,6]. These studies are motivated by the need for better understanding of multi-phase turbulent combustion processes as well as the demand for improving performance, stability, and emission control in industrial furnaces and propulsive systems such as gas turbine, ramjet engines, and space shuttle main engines.

The prediction of the local flow properties of spray flames requires the solutions of multi-phase dynamics, and accounts for complex interactions between the dispersed droplets and the continuous gas-phase flows. Various approaches have been suggested to model the interphase transport phenomena. The methodologies for the spray combustion computations are largely classified as the discrete droplet model, the statistical droplet model, and the two-fluid continuum model. Comparative performances for three approaches are well summarized in Ref.[6]. Among three models, the discrete droplet model has gained wide acceptance due to its computaional efficiency, the flexibility in handling poly-disperse spray, the convenient interphase coupling, and the elimination of numerical diffusion. With Eulerian-Lagrangian formulations in multi-phase flows, the stochastic separated flow(SSF) approach[5] categorized in the discrete droplet model is usually employed to account for the turbulence effects on interphase transport. In the present stochastic separated flow model, the mathematical formulation of the two-phase flow and combustion processes comprises the Eulerian conservation equation for the gas phase and the Lagrangian equations for the fuel droplets. The link between two phases is mathematically expressed in terms of liquid/gas-phase interaction source terms in the gas-phase equations. The governing gas-phase equations in Eulerian coordinate are solved by a time-marching multiple pressure correction procedure based on the operator-splitting technique. The droplet-phase equations in Lagrangian

coordinate are solved by a stochastic discrete droplet technique. The $k-\epsilon$ model is used to characterize the time and length scales of the gas phase turbulence for droplet dispersions and droplet/turbulence interactions. The present vaporization model includes the effects of variable thermophysical properties, non-unitary Lewis number in the gas-film, the Stefan flow effect, and the effect of internal circulation and transient liquid heating.

This study is mainly motivated to improve the physical submodels as well as to enhance the prediction capabilitiy over a wider range of fuel spray conditions and combustor geometries. In the following subsections, we adress several issues concerning the computational efficiency in the stochastic particle tracking method as well as the improvement of physical submodels of turbulence, combustion, vaporization, swirling effects, and dense spray effects.

1.2 Turbulent Particle Dispersion

In the stochastic separated flow(SSF) approach, each computational parcel represents a collection of liquid droplets having the same droplet characteristics and a random sampling technique is entailed for instantaneous gas flow properties based on a specified turbulence model and the resulting fluctuations are used in the droplet-phase Lagrangian computations for the droplet tracking. This stochastic process requires a large number of computational particles to produce satisfactory dispersion distributions even for rather dilute sprays. To circumvent this deficiency, Litchford and Jeng[7] proposed the dispersion width(group) approach in which each computational parcel represents a group of physical particles with a probability density distribution. This dispersion width model can account for the turbulent droplet dispersion within each group. Each group(width) grows due to the turbulent dispersion of droplets when the computational parcel travels in the Lagrangian coordinates. The mean position of each group, determined from a deterministic or stochastic Lagrangian tracking, is taken to represent the mean of its corresponding probability density function(PDF). The variance of each PDF is represented by a statistical mean-squared dispersion which depends on prior eddy interactions. Potential advantages of this method is to reduce the number of computational particles which represent the spray dynamics and to obtain grid-independent solutions

for two-phase flows regardless of grid-refinement in the underlying Eulerian gas-flow calculations. Other advantages may include better representations of "group" evaporation or "group" combustion models. The dispersion group model to be presented in this report is basically similar to the approach of Litchford and Jeng. However, the present procedure is somewhat different from the method proposed by Litchford and Jeng[7], in which the calculation of dispersion-related parameters needs summation of the entire time history. Furthermore, the present procedure is easy to program and requires less computer memory. To evaluate the present dispersion width transport model and to calibrate the stochastic simulation of particle-turbulence interactions, the computations were performed for the particle dispersion in nearly-homogeneous turbulence and a particle laden round jet in inhomogeneous turbulence. The present dispersion width transport model has successfully demonstrated the capability of accuratly representing dispersion in nearly-homogeneous and inhomogeneous turbulent flows with improved efficiency over the delta function SSF model.

1.3 Dilute Spray Models

In the dilute spray combustion models, the stochastic separated flow model is employed to account for the turbulent droplet dispersion, turbulence is represented by the $k-\epsilon$ model, and the combustion processes involves an irreversible one-step reaction at an infinite rate. The turbulent fluctuations on the mixture properties are introduced by the probability density function(pdf) approach. The centrifugal force terms associated with the swirl effects are also included in the gas-phase/droplet-phase equations. In the study, we evaluate the solution procedure and the physical submodels of turbulence, combustion, vaporization, swirling effects, and initial spray distributions. The present numerical model for the multi-phase turbulent reacting flows has been tested by applying it to predict the local flow properties in two axisymmetric, confined, swirling spray-combusting flows[36,37]. Example problems include the liquid-fuel combusting flows with a hollow cone spray and with a rotating cup atomizer. Special emphasis is given to the influence of the spray initial conditions and the inlet swirl strength which characterize the spray vaporization and the turbulent mixing. Two swirl numbers are considered to investigate the

influence of swirl on the droplet evaporation and trajectories, and the effects of droplet/ turbulence interactions in flow properties. The predictive capabilities of the present procedure have been demonstrated by comparisons with experimental data. The present numerical procedure correctly predicts the general features of spray-combustion flows and yields the qualitative agreement with experimental data. However, quantitative differences exist especially at near-burner locations, at near-wall regions, and along the combustion chamber centerline. The discrepancies observed in the results are attributed mainly to uncertainties in the initial spray size and velocity distributions and the droplet/wall impingement interaction, the single-step fast chemistry employed by the combustion model, and the deficiencies of the $k-\epsilon$ turbulence model dealing with the strong streamline curvature.

1.4 Dense Spray Models

One of the important aspects in spray combustion modeling is the dense spray effects which include atomization process, drop breakup, droplet collision and coalescence. Atomization process occurs on time and length scale too short to be resolved with practical computation grid sizes and time steps. Thus, atomization should be modeled as a sub-grid-scale process. To account for the dense spray effects, the present study employs the drop collision & coalescence model[8] and the Taylor analogy breakup(TAB) model[9]. In the drop collision model, the probability distributions governing the number and outcomes of the collisions between two drops are sampled randomly in consistency with the stochastic particle tracking method. The TAB model utilizes an analogy between an oscillating and distorting droplet and a spring-mass system. The present breakup model is based on the reasonable assumption that atomization and drop breakup are indistinguishable processes within a dense spray near the nozzle exit. Accordingly, atomiztion is prescribed by injecting drops which have a characteristic size equal to the nozzle exit diameter. Compared to Reitz's model[34], the TAB model has several advantages in terms of no need to input the spray angle, an easy introduction of liquid viscosity effects, and explicit informations of distortion and oscillation effects on the interphase exchange rates of mass, momentum, and energy. For non-evaporating, evaporating, and burning dense spray cases, the predictions show a reasonably good

agreement with available experimental results in terms of spray penetration, drop size distributions, and overall characteristics of the evaporating and burning spray. Future studies include the detailed comparison with the local properties available in the experiment and the implementation of a volume-of fluid (VOF) formulation for resolving the liquid volume displacement effects.

2. MATHEMATICAL MODELLING OF THE MULTI-PHASE FLOWS

All the gas-phase and liquid-phase processes are modeled by a system of unsteady, two-dimensional(axi-symmetric) equations. The gas-phase equation is written in an Eulerian coordinate whereas the liquid-phase is presented in Lagrangian coordinates. The two-way coupling between the two phases is described by the interaction source terms which represent the rates of momentum, mass and heat transfer. These equations are given below.

2.1 Basic Eulerian Equations

2.1.1 Mean Flow Equations

The density-weighted conservation equation of mass, momentum, and scalar variables in an Eulerian coordinate can be written as follows:

$$\frac{\partial \rho}{\partial t} + \frac{\partial}{\partial x_i}(\rho u_i) = S_{m,l} \tag{2.1}$$

$$\frac{\partial \rho u_i}{\partial t} + \frac{\partial}{\partial x_j}(\rho u_i u_j) = -\frac{\partial p}{\partial x_i} - \frac{\partial}{\partial x_j}[\rho \overline{u_i' u_j'}] + S_{u_i} + S_{u_i,l} \tag{2.2}$$

$$\frac{\partial \rho \phi}{\partial t} + \frac{\partial}{\partial x_i}(\rho u_i \phi) = -\frac{\partial}{\partial x_i}[\rho \overline{u_i' \phi'}] + S_\phi + S_{\phi,l} \tag{2.3}$$

where ρ is the time-mean density of the mixture, u_i and u_i' are the i component of the density-weighted mean and fluctuating part of the instantaneous velocity, ϕ and ϕ' are the density-weighted mean and fluctuating part of an instantaneous scalar quantities including the species concentrations and the total energy, p is the mean pressure, S_ϕ and $S_{\phi,l}$ represents the gas-phase source terms and the interaction source terms due to the fuel spray, respectively. Detailed expressions for these

source terms can be found in Refs.[10,11]. To close the system of equations, we need to model the unknown correlations, $\overline{u_i'u_j'}$ and $\overline{u_i'\phi'}$.

2.1.2 Turbulence Models

The two-equation effective diffusivity model is used to represent the turbulent characteristics. In the eddy diffusivity models, the turbulent fluxes, $\overline{u_i'u_j'}$ and $\overline{u_i'\phi'}$, are related to the mean flow gradients through the assumption of an isotropic eddy viscosity and a constant turbulent Prandtl or Schmidt number:

$$\overline{\rho u_i'u_j'} = -\mu_t(\frac{\partial u_i}{\partial x_j} + \frac{\partial u_j}{\partial x_i}) + \frac{2}{3}\delta_{ij}(\rho k + \mu_t\frac{\partial u_k}{\partial x_k}) \tag{2.4}$$

$$\overline{\rho u_i'\phi'} = -\frac{\mu_t}{\sigma_t}(\frac{\partial \phi}{\partial x_i}) \tag{2.5}$$

The eddy viscosity(μ_t) appearing in (2.4) and (2.5) is defined in terms of a characteristic turbulence length scale($k^{3/2}/\epsilon$) and a velocity scale ($k^{1/2}$), so that μ_t is given by

$$\mu_t = C_\mu\rho\frac{k^2}{\epsilon} \tag{2.6}$$

The turbulent kinetic energy, k, and its dissipation rate, ϵ, can be modeled from the turbulent transport equations:

$$\frac{\partial \rho k}{\partial t} + \frac{\partial}{\partial x_j}(\rho u_j k) = \frac{\partial}{\partial x_j}(\mu + \frac{\mu_t}{\sigma_k})\frac{\partial k}{\partial x_j} - \overline{\rho u_i'u_j'}\frac{\partial u_i}{\partial x_j} - \frac{\mu_t}{\rho^2}\frac{\partial \rho}{\partial x_j}\frac{\partial p}{\partial x_j} - \rho\epsilon \tag{2.7}$$

$$\frac{\partial \rho\epsilon}{\partial t} + \frac{\partial}{\partial x_j}(\rho u_j \epsilon) = \frac{\partial}{\partial x_j}(\mu + \frac{\mu_t}{\sigma_\epsilon})\frac{\partial \epsilon}{\partial x_j} + C_{\epsilon 1}\frac{\epsilon}{k}(\overline{\rho u_i'u_j'}\frac{\partial u_i}{\partial x_j} + \frac{\mu_t}{\rho^2}\frac{\partial \rho}{\partial x_j}\frac{\partial p}{\partial x_j}) - C_{\epsilon 2}\rho\frac{\epsilon^2}{k} \tag{2.8}$$

Here, terms involving $\frac{\partial \rho}{\partial x_j}$ in (2.7) and (2.8) are inserted to account for variable-density effects[12]. These terms originally come from the pressure-velocity correlation in the Reynolds stress equation. For reacting flows, these terms should account partially for the expansion effect on the flow field due to heat release from combustion.

2.1.3 Combustion Model

It is assumed that liquid fuel droplets act as distributed sources of fuel which evaporate to form a cloud of vapour. This implies that combustion process in spray flames can be treated as turbulent gaseous diffusion flames. Experimental evidence for this assumption can be found in Refs. 13. An idealized approach for physically-controlled diffusion flames is to invoke a fast-chemistry assumption which the chemistry is sufficiently fast and intermediate species do not play a significant role. In the turbulent diffusion flame model, the influence of turbulence on combustion is taken into account by relating the fluctuations of mass fractions. This implies that fuel and oxidizer can coexist in the same place but at a different time. The most convenient way to include the effect of turbulent eddies on thermochemical properties is via the introduction of the probability density function(pdf), $P(\xi, x_i)$. This function contains information of both mean(f) and variance of $(g = (f - \overline{f})^2)$ of the mixture fraction. These variables f and g can be obtained by solving the transport equations. The density-weighted mean values($\overline{\phi}$) of any property are evaluated by convoluting the property functions with a probability density fuction, $P(\xi, x_i)$:

$$\overline{\phi} = \int \phi(\xi) P(\xi, x_i) d\xi \tag{2.9}$$

Numerous probability density functions are available in the literatures. The present study adopts the β *pdf* which is known as the widely applicable one [11,12]. The detailed numerics of the β *pdf* are well described in Appendix B. The *double − delta pdf* procedures are also implemented in the program.

A modified eddy breakup model[14] is optionally incorporated in the present computer code. Using this model, the reaction rate is determined as follows: In an irreversible sigle-step chemical reaction, the mixing-controlled reaction rate[14] is given by

$$R_{mix} = A\rho \frac{\epsilon}{k} min(Y_f, \frac{Y_o}{s}) \tag{2.10}$$

where A is a model constant; s is the stoichiometric oxidant/fuel ratio; Y_f and Y_o are the mass fraction of the fuel and the oxidizer. To account for the ignition delay time, the chemical kinetics need to be considered. The chemically controlled reaction rate, R_{che}, is given by the usual Arrhenius formula[15].

$$R_{che} = A(\frac{\rho Y_f}{W_f})^a(\frac{\rho Y_o}{W_o})^b e^{(-\frac{E}{RT})} \tag{2.11}$$

The reaction rate, R_{fu} is determined from either of the mixing rates of the reactants or the chemical reaction rate, whichever slower.

$$R_{fu} = min(R_{mix}, R_{che}) \tag{2.12}$$

For simple one-step reaction of the hydrocarbon-air mixtures, there are five species participating the mixture composition. Once the mass fractions of fuel and oxdizer have been determined, the remaining species can be easily determined from the stoichiometric relations described in Appendix C.

2.2 Basic Lagrangian Equations

2.2.1 Droplet-Phase Equations

In this study, the spray is described by a discrete particle method formulated on a Lagrangian frame. This is essentially a statistical approach and requires tracking a sufficiently large number of computational particles. Each computational particle represents a number of droplets having equal location, velocity, size, and temperature. The governing equations for these are :

$$\frac{dx_i}{dt} = v_i \tag{2.13}$$

$$\frac{d\rho_d v_i}{dt} = \frac{u_i + u_i' - v_i}{\tau_i} + Fb_i \tag{2.14}$$

$$\frac{dr_p}{dt} = -\frac{m_{ev}}{4\pi {r_p}^2 \rho_d} \tag{2.15}$$

and

$$\frac{dT_d}{dt} = \frac{Q_L}{m_p C_{p,d}} \tag{2.16}$$

In equation (2.14), Fb_i represents the body force terms such as the gravity force and the centrifugal force. The particle relaxation time τ_i can expresses as:

$$\tau_i^{-1} = \frac{3}{8}\frac{\rho}{r_p} C_D |u_i + u_i' - v_i| \tag{2.17}$$

C_D is the drag coefficient given by

$$C_D = \frac{24}{Re_p}(1 + \frac{1}{6}Re_p^{\frac{2}{3}}); \quad \text{for} \quad Re_p < 1000$$
$$\text{and} \quad 0.424; \quad \text{for} \quad Re_p > 1000 \tag{2.18}$$

In which

$$Re_p = \frac{|u_i + u_i' - v_i|\rho d_p}{\mu} \tag{2.19}$$

In equation (2.15), the droplet evaporation rate is given by the Frossling correlation [16,17]

$$m_{ev} = 2\pi d_p(\rho D)(1 + 0.3Re_p^{\frac{1}{2}}Sc_d^{\frac{1}{3}})ln(1 + B_m) \tag{2.20}$$

In equation (2.16), the droplet temperature, which is assumed to be constant within the droplet, is found by using the heat energy Q_L :

$$Q_L = 4\pi r_p^2 Q_c - m_{ev}L \tag{2.21}$$

where L is the latent heat of vaporization, and Q_c is the heat conduction rate to the droplet surface per unit area. Q_c is given by the Ranz-Marshall correlation

$$Q_c = \frac{2K(T - T_d)}{d_p}(1 + 0.3Re_p^{\frac{1}{2}}Pr_d^{\frac{1}{3}})\frac{ln(1 + B_m)}{B_m} \tag{2.22}$$

The Schmidt number, Prandtl number and mass transfer number are defined respectively as

$$Sc_d = \frac{\mu}{\rho D}; \quad Pr_d = \frac{\mu C_p}{K}$$

and

$$B_m = \frac{Y_s - Y_\infty}{1 - Y_s}; \quad Y_\infty = \frac{\rho_f}{\rho} \tag{2.23}$$

The values of thermodynamical properties of gas such as K, C_p, D etc. are highly dependent on the temperature and fuel vapor mass fraction at which they are evaluated. A "one-third rule" [18] that utilizes a reference temperature equal to the droplet surface temperature plus one-third of the difference between the surrounding gas and droplet surface temperature is used. The same procedure is applied to the reference value for the fuel vapor mass fraction, in which Y_s is obtained from

$$Y_s = [1 + (\frac{P}{P_v} - 1)\frac{W_a}{W_f}]^{-1} \tag{2.24}$$

Here Y_s and P_v are the mass fraction and the fuel vapor pressure at the droplet surface, and W_f and W_a are the molecular weights of fuel and mixture, respectively. For a given T_d, P_v is estimated from the JANAF data bank [19]. The two-phase interaction source terms in the gas-phase governing equations are described in Appendix A. The droplet distribution models for the dilute sprays are also described in Appendix C.

In case of the droplet passage through the plane of symmetry, the droplet with same instantaneous properties and physical dimensions, but the mirror image velocity vector, is injected into the flowfield. On impingement on a wall, the droplets are assumed to bounce back with the reduced momentum[10].

2.2.2 Turbulence/Droplet Interactions

In this study, the spray is described by a discrete particle method formulated on a Lagrangian frame. To account for turbulence dispersion, we follow the concept of [7] of combining a normal (Gaussian) probability distribution for each computational particle. The instantaneous location of each computational paiticle is calculated by a stochastic Lagrangian tracking scheme. The governing equation for each computational particle is

$$\frac{dv_k}{dt} = \frac{u_k - v_k}{\tau_k} + F_{bk} \tag{2.25}$$

$$\frac{dx_k}{dt} = v_k \tag{2.26}$$

with

$$\tau_k^{-1} = \frac{3}{8}\frac{\rho}{\rho_p}\frac{C_D}{d_p}|u_k - v_k| \tag{2.27}$$

The location calculated by the above equations only represents the mean of each particle's corresponding probability function. The variance of each parcel pdf has to be calculated and the combined pdfs then represent the statistical distribution of particles with turbulent dispersion effects. To estimate the variance of the parcel pdf due to the turbulent particle dispersion, the turbulence-induced displacement and velocity can be splitted from equations (2.25) and (2.26):

$$\frac{dv'_k}{dt} = \frac{u'_k - v'_k}{\tau_k} \tag{2.28}$$

$$\frac{dx'_k}{dt} = v'_k \tag{2.29}$$

With the isotropic turbulence assumption, each component of u'_k is randomly chosen from a Gaussian distribution with standard deviation $u'_{krms} = \sqrt{\frac{2}{3}k}$. We first choose Δt_{ki} as the time step of the i^{th} interaction within the k^{th} eddy, which is smaller than the eddy lifetime, and integrate equations (2.28) and (2.29) to update particle fluctuating locations and velocities.

$$x'_{ki} = u'_{krms}\Delta t_{ki} + (v'_{k(i-1)} - u'_{krms})\tau_{k(i-1)}(1 - e^{\frac{-\Delta t_{ki}}{\tau_{k(i-1)}}}) \tag{2.30}$$

$$v'_{ki} = u'_{krms} + (v'_{k(i-1)} - u'_{krms})e^{\frac{-\Delta t_{ki}}{\tau_{k(i-1)}}} \tag{2.31}$$

We then sum up the m steps for which the particle fully interact with the k^{th} eddy,

$$\sum_{i=1}^{m} \Delta t_{ki} = \Delta t_k \tag{2.32}$$

The change of variance of a computational particle pdf within the k^{th} eddy is represented by a characteristic mean squared dispersion in the form:

$${\sigma_k}^2 = {\sigma_{k-1}}^2 + (\sum_{i=1}^{m} x'_{ki})^2 \tag{2.33}$$

In equation (2.33),σ_{k-1} is the existing variance of the particle pdf at the begining of the interaction within the k^{th} eddy. Since the time step within each turbluent eddy is fixed, the number of interaction within the eddy, m, varies across the calculation domain, the choice of time step Δt_{ki} and the related issues are discussed in detail in [24]. Figure 2.1 well describes this eddy interaction with the particles. The present procedure is easy to program and requires less computer memory. For each computational particle, we just need to store x'_{ki}, u'_{krms},v'_{ki}, and ${\sigma_k}^2$. This procedure when implemented in the current time-marching numerical method is somewhat different from the method of [7] in which the calculation of the current variance of each particle pdf is summed over the entire history of the effective time constants. In their recent study, truncation of unnecessary time history terms and the associated errors was discussed and additional computational efficency was obtained[35].

When convoluting pdf for a group of computational particles, the variances of eq.(2.33) must be normalized according to the total number of particles. The normalized particle variance can be written as

$$\hat{\sigma}_{yk} = K\frac{\sigma_{yk}}{\sqrt{N_t}} \tag{2.34}$$

Here, $\frac{\sigma_{yk}}{\sqrt{N_t}}$ represents the statistical uncertainty in the mean particle position, K is the correction factor to account for undersampling, and N_t is the total number of computational particles. When symmetry and reflective boundary condition exist in the calculation domain, a cumulative pdf distribution at any point in coordinate y, y is the distance from the particle to the axis or the reflective boundary, may be defined as:

$$P(y) = \int_{-y}^{y} \frac{1}{\sqrt{2\pi}\hat{\sigma}_{yk}} e^{\frac{-(y-y_p)^2}{2\hat{\sigma}^2_{yk}}} dy \tag{2.35}$$

Here, y_p is the instantaneous location of computational particles. After integration, the symmetric cumulative distribution function takes the form,

$$P(y) = 0.5[erf(\frac{y-y_p}{\sqrt{2}\hat{\sigma}_{yk}}) + erf(\frac{y+y_p}{\sqrt{2}\hat{\sigma}_{yk}})] \tag{2.36}$$

where

$$erf(x) = \frac{2}{\sqrt{\pi}}\int_o^x e^{-\zeta^2} d\zeta$$

In accordance with the approach of Litchford and Jeng[7], when the mean positions of computational particles is calculated by the deterministic tracking(u_k in Eqs.(2.25)-(2.27) is the mean gas velocity), this approach is described as the deterministic dispersion width transport(DDWT) model. For tracking using stochastic sampling of gas-phase turbulent velocity fluctuations(u_k in Eqs.(2.25)-(2.27) is the instantaneous gas velocity), the approach is described as a stochastic dispersion width transport(SDWT) model.

In the point delta function SSF model, the turbulence effects on droplet dispersion are simulated by a Monte Carlo method in the sense that a fluctuating velocity u'_k, where each component of u'_k is randomly chosen from a Gaussian distribution with standard deviation $\sqrt{\frac{2}{3}k}$, is added to the mean gas velocity. Thus

the turbulence is assumed to be isotropic. This type of simulation for the turbulent dispersion of droplets has been extensively used previously [20,21,22] for statistically stationary turbulent dispersed flows. Main differences in the implementations are the methods used to specify turbulence eddy properties and the methods for choosing the time of interaction of a particle with a particular eddy. The details of simulation procedures and also of various aspects associated within the interaction times can be found in Ref. [11,38].

2.2.3 Drop Breakup and Collision

The present study employs the TAB (Taylor Analogy Breakup) model proposed by O'Rourke and Amsden[9]. This model is based on an analogy between an oscillating and distorting droplet and a spring-mass system. The restoring force of the spring is analogous to the suface tension forces. The external force on the mass is analogous to the gas aerodynamic force. The damping forces due to liquid viscosity are introduced to this analogy. Compared to Reitz's model[34], the TAB model has several advantages in terms of no need to input the spray angle, an easy introduction of liquid viscosity effects, and the explicit informations of distortion and oscillation effects on the interphase exchange rates of mass, momentum, and energy. The major limitation of the TAB method is that only one oscillation mode can be tracked. However, in reality there exist many such modes in the Taylor analogy. Despite this limitation, good agreement between numerical results and experimentally observed bag/stripping breakup times has been reported. The droplet oscillation & breakup calculations require two normalized particle arrays(deformation and oscillation) which can be determined by the equation for the acceleration of the droplet distortion parameter. Occurance of droplet breakup, the Sauter mean radius(SMR), and oscillation velocity for the product drop depend on these two parameters and Weber number. The radius of the product drops is then chosen randomly from a chi-squared distribution with calculated SMR. Following breakup, the product drop has the same temperature with the parent drop, and its deformation and oscillating parameters are set to zero.

The drop collision model suggested by O'Rourke[8] is employed to calculate collision and coalescence among the dispersed liquid phase. The collision routine is

operatinging for the pair of particles if, and only if, they are in the same computational cell. For the collision calculation, the drops associated with each computation parcel are considered to be uniformly distributed throughout the computational cell where they are located. For all parcels in each computational cell, a collision frequency between drops between the parcel($parcel_1$) of larger drop radius(r_1) and the parcel($parcel_2$) of smaller drop radius(r_2) is obtained from the relationship in terms of the number of drops in $parcel_2$, the relative velocity between $parcel_1$ and $parcel_2$, the area based on $r_1 + r_2$, and the volume of computational cell. The probability with n collisions is assumed to follow a Poisson distribution based on a collision frequency and the computational time step. Using the probability informations, the collision impact parameters are stochastically calculated. If the collision impact parameter is less than a critical impact parameter, the outcome of every collision is coalescence. In opposite case, each collision is a grazing collision. The critical impact parameter depends on the drop radii, the relative velocity between drops, and the liquid surface tension coefficient.

3. NUMERICAL MODEL AND BOUNDARY CONDITIONS

The present method is based on the operator splitting technique[23] attempting to reach accurate transient solution after prescribed predictor- corrector steps for each time-marching step. The previous multiple pressure-correction method[11.27] is extended to to handle the strong nonlinear couplings arising in the multi-phase, fast-transient, and reacting flows. This method is non-iterative and applicable to all-speed flows. The additional scalar conservation equations such as species, and enery are incorporated into the same predictor-corrector sequence. Discretization of the gas phase governing equation uses the finite volume approach. To enhance the numerical stability, the implicit Euler scheme is employed in differencing the temporal domain. All the dependent and independent variables are stored at the same grid location and the variables at the finite control volume boundaries are interpolated between adjacent grid points. The discretizations have been performed on a general non-orthogonal curvilinear coordinate system with a second order upwind scheme for convection terms and the central differencing scheme for diffusion terms. The resulting discretized equations were solved by a conjugate gradient (CGS) solver. In

the present algorithm, each time step is divided into a one-predictor/two-corrector sequence. The strong coupling terms between particle and gas are evaluated by the same time splitting technique. Implicit coupling procedures are used to treat momentum exchanges to avoid the small timesteps. The unsteady solution procedure described above is somewhat different from the conventional PSIC(particle source in cell) procedure[25] in which global iterations are required. The method used here is non-iterative and time-accurate.

To improve the convergence and the numerical stability for the fast transient spray-combusting flows, all transport equations except the continuity equation are expressed in the advective form.

$$\frac{\rho^{n+1}-\rho^n}{\Delta t}+\frac{\partial}{\partial x_i}(\rho u_i)^{n+1}=S_{m,l} \tag{3.1}$$

$$\left[\frac{\rho^n}{\Delta t}\phi^{n+1}+(\rho u_i)^{n+1}\frac{\partial \phi}{\partial x_i}^{n+1}-\frac{\partial}{\partial x_i}(\Gamma_\phi\frac{\partial \phi}{\partial x_i}^{n+1})+\phi^{n+1}S_{m,l}\right]$$

$$=\frac{\rho^n}{\Delta t}\phi^n+S_\phi+S_{\phi,l} \tag{3.2}$$

By using operator-splitting method, the transport equations with the predictor-corrector procedure can be discretized as follows:

(a) Predictor step

Momentum(u^*):

$$(\frac{\rho^n}{\Delta t}-A_o)u_i^*=H^n(u_i^*)-\Delta_i p^n+S_{u_i}^n+S_{u_i,l}^n+\frac{\rho^n u_i^n}{\Delta t} \tag{3.3}$$

Scalar(ϕ^*):

$$(\frac{\rho^n}{\Delta t}-B_o)\phi^*=J^n(\phi^*)+S_\phi^n+S_{\phi,l}^n+\frac{\rho^n\phi^n}{\Delta t} \tag{3.4}$$

Here, the operators A_o, B_o, H, and J are constructed from the third-order upwind scheme for the convection terms and the central differencing scheme for the diffusion terms. To improve the numerical stability in multi-phase reacting flows, A_o and B_o may include the coefficient matrix resulting from the implicit treatment of the strong nonlinear source terms such as chemical reaction rates, turbulence source terms and multi-phase interaction source terms. The quantities $S_{u_i}^n$, $S_{u_i,l}^n$, S_ϕ^n , and $S_{\phi,l}^n$ are

determined from the existing flow fields. The general scalar dependent variables, ϕ may represent the enery, the mass fraction, and the turbulent transport quantities. In this stage, the velocity field(u_i^*) does not satisfy the continuity equation. The temperature T^* is calculated from the flowfield(energy, species,momentum) at the predictor step.

(b) First Corrector step

Momentum(u^{**}):

A new flowfield(u^{**}, p^*, ρ^*) are sought to satisfy the continuity equation:

$$\frac{1}{\Delta t}(\rho^* - \rho^n) + \Delta_i(\rho^* u_i^{**}) = S_{m,l}^n \tag{3.5}$$

and the discretized momentum equations are:

$$(\frac{1}{\Delta t} - \frac{A_o^n}{\rho^n})\rho^n u_i^{**} = H^n(u_i^*) - \Delta_i p^* + S_{u_i}^n + S_{u_i,l}^n + \frac{\rho^n u_i^n}{\Delta t} \tag{3.6}$$

Continuity equation (3.5) can be rewritten as:

$$\frac{1}{\Delta t}(\rho^* - \rho^n) + \Delta_i[\rho^n(u_i^{**} - u_i^*)] + \Delta_i[(\rho^* - \rho^n)u_i^{**}] = -\Delta_i(\rho^n u_i^*) + S_{m,l}^n \tag{3.7}$$

Subtracting Eq.(3.3) from Eq.(3.6) gives the velocity correction equation.

$$\rho^n(u_i^{**} - u_i^*) = -\rho^n Du^n[\Delta_i(p^* - p^n)] \tag{3.8}$$

Here,

$$Du^n = (\frac{\rho^n}{\Delta t} - A_o^*)^{-1}$$

Equations (3.7) and (3.8) are now used to derive the pressure correction equation. Thus, taking the divergence of Eq.(3.8) and substituting into Eq.(3.7) yields

$$[\frac{1}{\Delta t RT^*} + \Delta_i(\frac{u_i^*}{RT^*}) - \Delta_i(\rho^n Du^n \Delta_i)](p^* - p^n) =$$

$$-\Delta_i(\rho^n u_i^*) + S_{m,l}^n + (\frac{1}{RT^n} - \frac{1}{RT^*})\frac{p^n}{\Delta t} + \Delta_i[(\frac{1}{RT^n} - \frac{1}{RT^*})p^n u^*] \tag{3.9}$$

Equation (3.9) can be solved for the corrected pressure, p^*. The density(ρ^*) is calculated from the equation of state. The velocities(u_i^{**}) are computed from Eq.(3.8).

Scalar(ϕ^{**}):

These new flowfield(u_i^{**},ρ^*) satisfying the continuity equation (3.5) are used to update the B coefficient.

$$(\frac{\rho^n}{\Delta t} - B_o^*)\phi^{**} = J^*(\phi^*) + S_\phi^* + S_{\phi,l}^n + \frac{\rho^n \phi^n}{\Delta t} \tag{3.10}$$

The temperature T^{**} is calculated from the corrected flowfield(enegy, species,momentum).

(c) Second Corrector step

Momentum(u^{***}):

A new flowfield(u^{***}, p^{**}, ρ^{**}) are sought to satisfy the continuity equation:

$$\frac{1}{\Delta t}(\rho^{**} - \rho^n) + \Delta_i(\rho^{**} u_i^{***}) = S_{m,l}^n \tag{3.11}$$

Subtracting Eq.(3.5) from Eq.(3.11) yields

$$\frac{1}{\Delta t}(\rho^{**} - \rho^*) + \Delta_i[\rho^*(u_i^{***} - u_i^{**})] + \Delta_i[(\rho^{**} - \rho^*)u_i^{***}] = 0 \tag{3.12}$$

The discretized momentum equations are:

$$(\frac{\rho^n}{\Delta t} - A_o^*)u_i^{***} = H^*(u_i^{**}) - \Delta_i p^{**} + S_{u_i}^n + S_{u_i,l}^n + \frac{\rho^n u_i^n}{\Delta t} \tag{3.13}$$

Subtracting Eq.(3.6) from Eq.(3.13) yields

$$u_i^{***} - u_i^{**} = Du^*[(A_o^* - A_o^n)u_i^{**} + H^*(u_i^{**}) - H^n(u_i^*)] - Du^*[\Delta_i(p^{**} - p^*)] \tag{3.14}$$

Here,

$$Du^* = (\frac{\rho^n}{\Delta t} - A_o^*)^{-1}$$

By substituting Eq.(3.14) into Eq.(3.12), the corrected pressure equation is obtained:

$$[\frac{1}{\Delta t RT^{**}} + \Delta_i(\frac{u_i^{**}}{RT^{**}}) - \Delta_i(\rho^* Du^* \Delta_i)](p^{**} - p^*) =$$
$$\Delta_i[\rho^* Du^*[(A_o^* - A_o^n)u_i^{**} + H^*(u_i^{**}) - H^n(u_i^*)]]$$

$$+(\frac{1}{RT^*}-\frac{1}{RT^{**}})\frac{p^*}{\Delta t}+\Delta_i[(\frac{1}{RT^*}-\frac{1}{RT^{**}})p^*u^*] \tag{3.15}$$

Using the corrected pressure(p^{**}), the density(ρ^{**}) is obtained from the equation of state. The velocities(u_i^{***}) are computed from Eq.(3.15).

Scalar(ϕ^{***}):

These new flowfield(u_i^{***},ρ^{**}) satisfying the continuity equation (3.11) are used to update the B coefficient.

$$(\frac{\rho^n}{\Delta t}-B_o^{**})\phi^{***}=J^{**}(\phi^{**})+S_\phi^{**}+S_{\phi,l}^n+\frac{\rho^n\phi^n}{\Delta t} \tag{3.16}$$

The temperature T^{***} is calculated from the updated flowfield(energy, species,momentum). The updated flowfield(ρ^{**}, p^{**},u_i^{***}, T^{***}, and ϕ^{***}) are taken to represent the field values at the next time step(n+1). This completes the sequence in the solution of the equation over the time-step.

In the present pressure-based method, the left hand side of the corrected pressure equations written in Eq.(3.9) and Eq.(3.15) involve a convection term which can properly takes into account the hyperbolic nature of supersonic flows, and enables capturing shock waves. A recently developed non-iterative PISO method[39] does not include this convective term due to the inconsistent treatment of density in the momentum equations. Compare to our previous pressure-based method[27], this new method allows the consistent discretization of continuity equation and is more suitable for the fast-transient reacting flow at all speeds. For the steady state calculations, the present procedure can be simplified by freezing the coefficient matrix(A_o, B_o).

For the subsonic inlet boundary. the entropy and the total pressure are specified. The axial velocity components are obtained by the extrapolation and the vertical velocity components are determined by enforcing the vorticity to vanish at the upstream boundary. At symmetry, the normal grdients of all scalar variables and the radial velocity component are zero. At the supersonic outlet, all dependent variables are extrapolated from the interior. The wall was assumed to be adiabatic.

4. RESULTS AND DISCUSSIONS

To evaluate the present dispersion width transport model and to calibrate the stochastic simulation of particle-turbulence interactions, the computations were performed for the solid particle dispersion in nearly-homogeneous turbulence and a particle laden round jet in inhomogeneous turbulence. The validation cases for the dense spray models include non-evaporating, evaporating, and burning sprays.

4.1 Turbulent Particle Dispersion

4.1.1 Nearly-Homogeneous Turbulent Dispersion

The particle dispersion experimental setup of Snyder and Lumley [28] in a grid-generated turbulent flow was used for evaluating the present dispersion PDF transport model. Particle densities and sizes are chosen to examine the phenomena in which the eddy lifetime controls interaction times (46.5 μm diameter hollow-grass) , the transit time controls interaction times (87.0 μm corn pollen), or the controlling-interaction times undergo transition from transit time to eddy life time (87.0 μm solid glass). In this experiment, fluid turbulence intensities and length scale information were measured. The particle calculations were started at the experimental particle injection point of $x/m = 20$ (m is a 2.54-cm-square mesh). The particle velocity was assumed equal to the mean fluid velocity of 6.55 m/sec. For the delta function SSF computations, 5,000 computational particles were sampled to calculate the resulting mean squared dispersion with respect to time. For the DDWT computations, a single parcel in a deterministic trajectory along the centerline was sampled to evaluate the mean squared dispersion representing the variance of the parcel PDF by using the related parameters for each eddy interaction.

Figure 4.1 shows comparison of the predicted and measured particle dispersion with respect to time. The DDWT results show good agreement with the SSF results for light, medium, and heavy particles. Both models also show favourable agreement with the experimental data. These numerical results indicate that the DDWT model with a single computational parcel following the deterministic trajectory demonstrates the efficiency, the accuracy, and the overall prediction capability for this nearly-homogeneous turbulent flow.

4.1.2 Inhomogeneous Turbulent Dispersion

The next example problem is a particle laden round jet[29] in which the turbulence is inherently inhomogeneous. The turbulent gas-phase transport properties are provided by using the $k-\epsilon$ model. Figures 4.2 and 4.3 show the particle concentration profiles of the delta function SSF model and the SDWT model for 50 and 200 computational parcels, at various levels of the correction factor, and at several axial locations. 10,000 particles are sampled for the delta function SSF computations. Using the 10,000 particles in the SSF model, there is still evidence of slight undersampling. However the distribution is relatively smooth and is taken here as a good approximation to the theoretical profile. The 50 parcel case of SDWT model shown in Figure 4.2 is very sensitive to the level of the correction factor especially for upstream regions due to undersampling. By increasing the correction factor, K in eq.(13), the uncertainty level in the mean increase the dispersion and smooth the profile considerably. In Figure 4.3, the zero correction factor case(K=0) corresponds to the delta function SSF case using 200 computational particles. The computed profile of the SSF case for 200 particle samples is very irregular and shows oscillatory distribution. The 200 parcel case of SDWT model shown in Figure 4.3 is less sensitive to the correction factor since there is less uncertainty in the mean because of increased sampling. In Figure 4.4, the SDWT results with 200 parcels and K=4 shows favourable agreement with the delta function SSF with 10,000 computational particles. These numerical results clearly indicated that the SDWT model has the capability of accuratly representing dispersion in inhomogeneous turbulent flows with improved efficiency over the delta function SSF model.

4.2 Dilute Spray Combusting Flows

The present numerical model for the multi-phase turbulent reacting flows has been tested by applying it to predict the local flow properties in two axisymmetric, confined, swirling spray-combusting flows[36,37].

4.2.1 Hollow-Cone Kerosene Spray Flames

The combustor geometry of the first test case is shown in Fig. 4.5. Experimental data for temperature, axial and tangential velocity components were obtained from measurement of Khalil et. al.[36]. The inlet conditions and the initial droplet

size distribution are given in Table 1. Liquid kerosene was used as fuel and the air/fuel mass ratio was fixed at 20.17.

In the present study, two swirling numbers(S=0.72 and 1.98) were considered to investigate the influence of swirl on the droplet evaporation & burning characteristics. Fig. 4.6-4.8 show the general flow pattern such as the predicted droplet trajectories, velocity vectors, and temperature contours of two swirl cases. In the lower swirl case(S=0.72), large portion of droplets survive in the central recirculation zone and continue to evaporate in the far downstream region. In the high swirl case(S=1.98), most of small droplets are trapped in the recirculation zone and evaporate there, producing intensive burning and high temperature in this region. With increasing swirl, the droplet spreading increases due to the droplet dispersion and the increased particle centrifugal force term. In addition, the larger central recirculation zone corresponding to the higher inlet swirl is contributed to recirculate more hot combustion gas from downstream and to increase the temperature at near inlet regions.

The predicted and measured temperature profiles for two swirl cases are shown in Fig. 4.9 and 4.10. The siginificant discrepancies in near-wall regions mainly result from the uncertainties of droplet/wall impingement process. However, the deviations in other locations are associated with the deficiencies of turbulence and combustion models, the unreliable informations of the inlet droplet size & velocity distribution, and the potential errors in inlet swirl profiles and inlet turbulence length scale. It is observed that the temperature profiles of the high swirl case are more uniform than those of the low swirl case. Radial profiles of axial velocity velocity for S=0.72 and 1.98 are shown in Fig. 4.11 and 4.12. The present numerical model underpredicts the magnitude of the reverse flow velocities. The poor performance of the present numerical model in predicting the size of central recirculation zone and the reverse velocity is partly attributed to the deficiency of $k-\epsilon$ model based on the isotropic assumption. The predicted and measured tangential velocities for two swirl cases are presented in Fig. 4.13 and 4.14. The significant deviation close to the inlet is likely caused by the incorrect distribution of inlet swirl velocities. In the present study, the inlet swirl velocities are obtained from the

estimated axial angular momentum flux. The rapid decay of the tangential velocity to the solid body rotation close to the centerline could be tied with the errors in the prediction of reverse velocities.

4.2.2 Spray Flame with a Rotating-Cup Atomizer

Fig. 4.15 shows the liquid-fueled combustor with a rotating cup atomizer[37] which is capable of producing a near-monodisperse spray. This small near-monosized spray allows the relatively accurate representation of the droplet initial conditions and eliminates the uncertainties in the droplet/wall impingement process. The gas-phase inlet boundary conditions and the droplet intial conditions(droplet size & velocity distributions) were estimated from measurement of El-Banhawy and Whitelaw[37]. Liquid kerosene was used as fuel and the fuel/air mass ratio was fixed at 0.0228. In present study, computaions were carried out for a test condition with the swirl number(S=1.2) and the droplet diameter($r_k = 47\mu m$). Since the experimental data provided the limited informations for gas-phase inlet and droplet injector conditions, there are some potential errors associated with the inlet swirl profiles, and the initial distributions for droplet size and velocity. In this test case with small droplet size, considerable change in droplet velocity can occur in the short distance between the injection location and the measurement station; therefore, some error might be introduced in the droplet initial velocity specifications. Based on the experimental data, the droplet size distributions were specified with the near-monosized droplets($47\mu m$, 70 % fuel mass flow rate) and the smaller satellite droplets ($24\mu m$, 30 % fuel mass flow rate).

The predicted droplet trajectories, velocity vectors, and temperature conturs are shown in Figure 4.16-4.18. It is observed that two high-temperature regions exist in the shear layer around the recirculation zone, and the main flame region around the central recirculation zone and downstream of the fuel spray. Numerical results indicate that these high-temperature regions are characterized by the trapping of smaller droplets, high evaporation rate, and intensive turbulent mixing and chemical reaction. Figure 4.19-4.21 show the predicted and measured radial profiles of temperature, mass fractions of carbon dioxide (CO_2) and oxygen(O_2) at four axial locations. The numerical results shows the qualitative agreement with the

experimental data. However, quantitative differences exist in the profiles of temperature and corresponding chemical concentrations. The sigificant discrepancies close to the inlet(X/D=0.254,0.510) are mainly attributed to the incorrect specification of swirl velocity profile, the insufficient turbulent mixing predicted by the $k-\epsilon$ turbulence model, and the neglect of intermediate species such as soot and carbon monoxide(CO) associated with the single-step fast chemistry model. In these regions, the overpredicted CO_2 mass fractions can be partly explained by the existence of the high CO mass fractions($\simeq$ 10%) observed in measurement. Due to the relatively high heat release rate of CO_2, the calculated temperatures are much higher than the measured values. At the far downstream regions(X/D=2.9) of the spray flame, the differences between the calculated and measured temperature values decreases to around 100 K.

4.3 Dense Spray

4.3.1 Non-Evaporating Solid-Cone Spray

The solid-cone spray measurements of Hiroyasu and Kadato[30] were used to validate the present numerical dense spray model which includes collison, coalescence, and breakup models described above. Liquid fuel is injected through a single hole nozzle into constant pressure, room-temperature nitrogen. Spray tip penetration and drop sizes were measured from photographs of the backlighted spray. The test conditions are given in Table 2 (SMD is the average over the spray cross-section 65 mm downstream of the nozzle). The nozzle diameter was 0.3 mm and the present computations used tetradecane for the liquid fuel(the experiments used a diesel fuel oil with physical properties close to tetradecane).

A computational domain of 20 mm in radius and 120 mm in length was discretized by a 25 radial and 45 axial grid. The mesh spacing was nonuniform with refinement on the centerline and close to the injector. The smallest cell is 0.5 mm radially and 1.5 mm axially. Since this dense spray calculation is sensitive to the grid resolution, the fine grid was used to obtain a grid-independent solution. The number of computational parcels at steady-state conditions was between 1000 and 1500, and the number was varied with the back pressure. The present numerical

results did not change appreciably when this parcel number was varied. The initial turbulent quantities were assumed as the small values($k = 1 \text{ x } 10^{-3} m^2/s^2, \epsilon = 4 \text{ x } 10^{-4} m^2/s^3$). The numerical results were insensitive to these initial values.

The spray parcel distribution for three sprays is shown in Figure 4.22. This plot indicates that the spray tip penetration and the core length decrease with the increase of the gas density. Figure 4.23 shows the predicted and measured spray tip penetration versus time. It can be seen that there is reasonably good agreement between the prediction and the measurement . In the present computations, the spray tip was defined to be the location of the leading spray drop parcel. It is necessary to note that a far-field spray penetration is not a sensitive indicator of model performance. Previous studies[26,31] indicated that a far-field spray penetration is mostly influenced by the turbulence diffusivity. However, a near-field spray penetration could be more sensitive to the physical submodels such as breakup and collision. Figure 4.24 shows the variation of SMD with axial distance from the injector. The three solid data at 65 mm correspond to the measurements. The computed drop size is a time average over the spray cross-section at each axial location. At the nozzle exit, the drop diameter is equal to the nozzle diameter, 0.3 mm. Generally these curves can be broken into two sections. Close to the injector, the drop size decreases rapidly due to drop breakup. Further downstream, the drop size increases gradually due to drop coalescence. In the low gas pressure case(1.1 MPa), the drop size remains relatively uniform after initial breakup region and then increases slightly in the far-downstream region. For the high pressure cases(3.0 and 5.0 MPa), the drop size increases largely in far-downstream region, because higher gas densities promote collisions and coalescence. This trend is also observed in the measuments. The predicted drop sizes at 65 mm are qualitatively agreed with the experimental data for all three cases. The discrepancy could be associated to the fact that the experimental sprays were pulsed while the computations assumed a constant pressure injection for the entire computational time period.

4.3.2 Non-Evaporating Hollow-Cone Spray

The hollow-cone spray tip penetration data of Shearer and Groff[32] have been used for the model validation. In the experiment, the liquid is injected into quiescent

room-temperature nitrogen at $P = 550kPa$. The numerical timestep is used as $2.5\mu s$ and about 2000 spray parcels are used in the computation. The experimental spray cone angle is 60 degrees, and the flow rate 0.0165 mL/injection with four pulses, each of duration about 0.58 ms. The computational injection velocity are set to the experimental spray tip velocity($60m/s$) measured from the movie pictures in the early stage of the injection. The test condition is listed in Table 3.

Figure 2.25 shows the spray parcel distribution and the velcocity vectors, and the predicted and measured spray tip penetration versus time. The numerical results indicate that turbulence has a relatively small effect on penetration in a hollow-cone spray because radial spreading due to inertia is dominant. The gas velocity vectors indicate the presence of a vortex near the head of the spray, which curls the spray tip toward the outside of spray. A substantial region of strong inward flow in the center of the cone near the injector was also observed. These flow patterns and spray shapes compared quite favorably with the experimental observations[32]. In Figure 2.26, the predictions reasonably agree with the experimental spray tip penetration.

4.3.3 Evaporating and Burning Solid-Cone Spray

The evaporating and buring solid-cone spray measurement of Yokoda et. al.[33] have been used to validate the present numerical dense spray model. Liquid fuel(tridecane) is injected through a sigle hole nozzle into high-pressure, high-temperature nitrogen or air. The test conditions for evaporating and burning sprays are given in Table 4. The nozzle diameter was 0.16 mm. A computational domain of 20 mm in radius and 100 mm in length was discretized by a 21 radial and 44 axial grid. The mesh spacing was nonuniform with refinement on the centerline and close to the injector. The number of computational parcels at steady-state conditions was between 500 and 700. Due to the numerical reasons, the initial turbulent quantities were assumed as the small values. The upstream boundary is treated as a solid wall, and other boundary are treated as open boundaries.

Figure 2.27 shows the spray parcel distribution and the contours of the fuel mass fraction for evaporating sprays. These results show that the spray penetration increase with respect to time at early period of injection, however the penetration become nearly constant after $t = 0.2ms$ due to evaporation. Even though

the liquid drop does not penetrate more, the evaporated fuel vapor continuously penetrate with respect to time. Comparisons of the computed and experimental spray penetration versus time are shown in Figure 2.28. The present spray penetration distance agrees well with the measured results[33]. Figure 2.29 and 2.30 shows the spray parcel distribution, the contours of the fuel mass fraction, temperature, and oxygen mass fraction at different times of injection for burning sprays. The computed configuration of a burning spray flame has the overall agreement with the measure ones. In the experimental study, a considerable level of soot was observed near the spray tip where the equivalence ratio is low and the temperature is high due to the progressed turbulent mixing. Therefore, the soot model should be incorporated to improve the prediction capability of the present burning dense spray model. Future studies may include the detailed comparison with the local properties available in the experiment.

5. CONCLUSIONS

The numerical models have been developed for the analysis of dilute and dense spray-combusting flows. From the present numerical studies, the following conclusions are drawn in general:

1. Present implementation of the dispersion width transport model has successfully demonstrated the capability of accuratly representing dispersion in nearly-homogeneous and inhomogeneous turbulent flows with improved efficiency over the delta function SSF model.
2. A numerical model for the prediction of the statistically stationary spray-combusting flows is evaluated by comparison with the available experimental data. The present numerical procedure correctly predicts the general features of spray-combustion flows and yields the qualitative agreement with experimental data. However, quantitative differences exist especially at near-burner locations, at near-wall regions, and along the combustion chamber centerline. The discrepancies observed in the results are attributed mainly to uncertainties in the initial spray size and velocity distributions and the droplet/wall impingement interaction, the single-step fast chemistry employed by the combustion model, and the deficiencies of the $k-\epsilon$ turbulence model dealing with the strong

streamline curvature. To improve the prediction capabilities of the present numerical procedure, the future works must include the consistent studies of non-evaporating, evaporating, and burning sprays by utilizing the non-isotropic turbulence model such as the algebraic stress model and the second-moment closures, and the multi-step finite chemistry model.

3. For non-evaporating, evaporating, and burning dense spray cases, the predictions show a reasonably good agreement with available experimental results in terms of spray penetration, drop sizes, and overall configuration of a burning-spray flame. To improve the prediction capabilities and efficiencies of the numerical and physical models, future works must include the extensions of the dispersion width transport model to non-evaporating, evaporating, and burning dense sprays, the incorporation of supercritical vaporization model, the incorporation of soot model and further refinement of atomization and breakup models.

6. RECOMMENDATIONS

The following recommendations are intended as suggestions for improvements and extensions of the present spray combustion modelling. The numerical and physical modelling studies are need for the following tasks.

- Implementation of computationally efficient parcel PDF approach for multiphase, turbulent, evaporating, and combusting flows.
- Development of strong interphase coupling procedure by combining multiple pressure correction procedure and Volume of Fluid(VOF) method.
- Implementation of equilibrium and non-equilibrium chemitry packages for efficient transient reacting flow calculations.
- Optimization and adaptation of breakup and coalescence procedure.
- Atomization modeling in conjunction with multi- step pressure correction methodology.
- Incorporation of turbulence modulation effects by droplets.
- Incorporation of wall/droplet impingement process.

- Incorporation of supercritical vaporization model.

The validations and the applications of the proposed spray combustion models will be consistently studied for the following cases:

- Benchmark solution for non-evaporating, evaporating, and burning dense sprays.
- Unsteady flame propagation in a two-dimensional spray with transient droplet vaporization.
- Numerical analysis of SSME injector atomization and combustion process.
- Application to bipropellant spray combustion.
- Numerical simulation of combusting flows with supersonic droplet injection.

Acknowledgements

The authors would like to express their appreciation to Dr. T.S. Wang of NASA/MSFC for active participation and critical comments. Acknowledgement is extended to Mr. R.J. Litchford for valuable discussions on the parcel PDF modelling. The authors also wish to acknowledge the CRAY CPU time supplied by the Alabama Supercomputer Network through UAH.

REFERENCES

1. Asheim, J.P. and Peters, J.E.(1989), "Alternative Fuel Spray Behavior", *J. Propulsion and Power*, **5**, pp. 391-398.
2. Aggarwal, S.K.(1988), "Ignition Behavior of a Dilute Vaporizing Multicomponent Fuel Spray", AIAA-88-0635, 26th Aerospace Sciences Meeting, Reno, Nevada, Jan.
3. Sirignano, W.A.(1983), "Fuel Droplet Vaporization and Spray Combustion" , *Prog. Energy Comb. Sci.*, **9**, pp. 291-322.
4. Law, C.K.(1982), "Recent Advances in Droplet Vaporization and Combustion", *Prog. Energy Comb. Sci.*, **8**, pp. 171-201.
5. Faeth, G.M.(1987), "Mixing, Transport and Combustion in Spray", *Prog. Energy Comb. Sci.*, **13**, pp. 293-345.
6. Sirignano, W.A.(1986), "The Formulation of Combustion Models: resolution compared to droplet spacing," *ASME Journal of Heat Transfer*, **108**, pp. 633-639.
7. Litchford, R.J. and Jeng, S.M.(1991), "Efficient Statistical Transport Model for Turbulent Particle Dispersion in Sprays", *AIAA J.*, **29**, no. 9, pp. 1443-1451.
8. O'Rourke, P.J.(1981) "Collective Drop Effects on Vaporing Liquid Sprays", Los Alamos National Laboratory report LA-9069-T.
9. O'Rourke, P.J.(1987), "The TAB Method for Numerical Calculation of Spray Droplet Breakup", SAE Technical Paper 872089.
10. El Banhawy, Y., and Whitelaw, J.M.(1980), "Calculation of the Flow Properties of a Confined Kerosene-Spray Flames", *AIAA J.*, **18**, pp. 1503-1510.
11. Kim, Y.M., Shang, H.M., and Chen, C.P.(1991), "Non-Isotropic Turbulence Effects on Spray Combustion", AIAA Paper 91-2196, 27th Joint Propulsion Conference, Sacramento, CA, June 24-26.
12. Jones, W.P.(1980), "Models for Turbulent Flows with Variable Density and Combustion", in W. Kollman (ed.), Prediction Method for Turbulent Flows, Hemisphere Publishing, London, pp. 379-422.

13. Tuttle, J.H., Shisler, R.A., and Mellor, A.M.(1976), "Investigation of Liquid Fueled Turbulent Diffusion Flames", *Combustion Science and Technology*, **14**, pp. 229-241.

14. Magnussen, B.F. and Hjertager, B.H.(1977), "On Mathematical Modeling of Turbulent Combustion With Special Emphasis on Soot Formation and Combuation", 16^{th} Symposium on Combustion, p. 719.

15. Westbrook, C.K. and Dryer, F.L.(1984), "Chemical Kinetic Modelling of Hydrocarbon Combustion," *Prog. Energy Comb, Sci.*, Vol.10, pp. 1-57.

16. Frossing, N.(1938), "On the Evaporation of Falling Droplets", *Gerlands Beltrage Zur Geophysik*, **52**, pp. 170-216.

17. Abramzon, B. and Sirignano(1988), "Droplet vaporization model for spray combustion calculations," AIAA Paper 88-0636, 26th Aerospace Science Meeting, Reno, Nevada.

18. Hubbard, G.L. et al.(1975), "Droplet Vaporization : Effects of Transient and Variable Properties", *Int. J. Heat and Mass Transfer*, **18**, pp. 1003- 1008.

19. Stull D.R. and Prophet H.(1974), "JANAF Thermochemical Table", 2nd edition, N.W. Chase et al., *J. Phys. Chem. Ref. Data*, **3**, 311.

20. Gosman, A.D. and Ioannides, E.(1981), "Aspects of Computer Simulation of Liquid Fueled Combustors", AIAA 81-0323.

21. Fashola, A. and Chen, C.P.(1990), "Modeling of Confined Turbulent Fluid-Particle Flows Using Eulerian and Lagrangian Schemes", *Int. J. Heat and Mass Transfer*, **33**, pp. 691-700.

22. Shuen, J.S. et al(1985). "Structure of Particle-Laden Jets : Measurements and Predictions", *AIAA J.*, **23**, pp. 396-404.

23. Issa, R.I.(1985), "Solutions of the Implicitly Discretized Fluid Flow Equations by Operator Splitting", *J. Comp. Physics*, **62**, pp. 40-65.

24. O'Rourke, P.J.(1989), "Statistical Properties and Numerical Implementation of a Model for Droplet Dispersion in a Turbulent Gas", *J. Comp. Physics*, **83**, pp. 345-360.

25. Crowe, C.T., Sharma, M.P. and Stock, D.E.(1977), "The Particle Source in Cell Method for Gas-Droplet Flows", *J. Fluid Eng.* **99**, pp. 325-332.

26. Chen, C.P., Shang, H.M. and Jiang, Y.(1990), "A Novel Gas-Droplet Numerical Method for Spray Combustion", Eigth Liquid Rocket Engine CFD Working Group Meeting, NASA-MSFC, April 17-19, 1990, to be appeared in the *Int. J. Numer. Meth. Fluids*, 1992.

27. Chen, C.P., Jiang, Y., Kim, Y.M., and Shang, H.M.(1991) "MAST - A Multi-Phase All-Speed Transient Navier-Stokes Code in Generalized Coordinates", NASA Contract Report, NAG8 -092, Dec., 1991

28. Snyder, W.H. and Lumley, J.L.(1971), "Some Measurements of Particle Velocity Autocorrelation Functions in a Turbulent Flow", J. Fluid Mech., 48, pp. 41-71.

29. Yuu, S., Yasukouchi, N., Hirosawa, Yasuo, and Jotaki, T.(1978), "Particle Turbulent Diffusion in a Dust Laden Round Jet", *AIChE Journal*, **24**, No. 3, pp. 509-519.

30. Hiroyasu, H. and Kadato, T.(1974), "Fuel Droplet Size Distribution in Diesel Combustion Chamber," SAE Paper 740715.

31. Dukowicz, J.K.(1980), "A Particle-Fluid Numerical Model for Liquid Sprays", J. Comp. Physics, 35, pp. 229-253.

32. Shearer, A.J. and Groff, E.G.(1984), "Injection System Effects on Oscillating-Poppet-Injector Sprays," Proceedings of the ASME Diesel and Gas Engine Power Division Conference, New York, 1984, pp. 33-42.

33. Yokota, H., Kamimoto, T., and Kobayashi, H.(1988), "A Study of Diesel Spray and Flame by an Image Processing Technique, *Bulletin of JSME*, **54**, p. 741.

34. Reitz, R.D. and Diwaker, R.(1987), "Structure of High Pressure Fuel Sprays," SAE Paper 870598, 1987

35. Litchford, R.J. and Jeng, S.,M.(1992), "On the Efficiency of a Statistical Transport Model for Turbulent Particle Dispersion," to be appeared in *AIAA J.*, 1992

36. Khalil, K.H., El-Mahallawy, F.M., and Moneib, H.A., "Effect of Combustion Air Swirl on the Flow Pattern in a Cylindrical Oil Fired Furnace", Sixteenth

Symposium on Combustion, The Combustion Institute, Pittsburgh, PA, pp. 135-143, 1977

37. El-Banhawy, Y. and Whitelaw, J.H., "Experimental Study of the Interaction Between a Fuel Spray and Surrounding Combustion Air," Combustion and Flame, 42, No. 3, pp. 253-275, 1981
38. Kim, Y.M., Shang, H.M., Chen, C.P., Ziebarth, J.P., and Wang, T.S., "Numerical Studies on Dilute and Dense Sprays," AIAA Paper 92-0223, 30th Aerospace Science Meeting, Reno, Nevada.
39. Issa, R.I. et. al., "Solution of the Implicitly Discretized Reacting Flow Equations by Operator-Splitting," *J. Comp. Phy.* **93**, pp. 388-410, 1991.

Table 1. Gas-phase B.C. and droplet-phase I.C.

Air Mass Flow Rate	**355 kg/hr**
Air/Fuel Ratio	**20.17**
Inlet Air Temperature	**310 K**
Droplet Distribution	**Rosin-Rammler**
Sauter Mean Diameter	**127 μ m**
Droplet Size Range	**10 ~ 290**
Number of Size Range	**15**
Axial Droplet Velocity	**11 m/s**
Tangential Droplet Velocity	**6.1 m/s**
Radial Droplet Velocity	**0.5 ~ 2.5 m/s**
Droplet Temperature	**310 K**

Table 2. Test Conditions for the Measurement of Hiroyasu and Kadota

Nozzle diameter: 300 μm Injection Pressure: 9.9 MPa

Case	Pgas (MPa)	ρgas (kg/m³)	Vinj (m/s)	$\dot{M}_{inj}$ (kg/s)	SMD (μm)
1	1.1	12.36	115.80	0.00688	42.4
2	3.0	33.70	102.54	0.00609	49.0
3	5.0	56.17	86.41	0.00513	58.8

Table 3. Test Conditions for the Measurements of Shearer and Groff.

Pgas (kPa)	ρgas (kg/m³)	Vinj (m/s)	VOLinj (ml/inj)	Cone Angle (deg)
550	6.36	60	0.0165	60

Table 4. Test Conditions for the Measurement of Yokota et. al.

Case	Pinj (MPa)	Pgas (MPa)	Tamb (K)	Minj (kg/s)	Atmosphere
Evaporating Spray	30	3.0	900	0.00326	N_2
Burning Spray	30	3.0	900	0.00326	Air

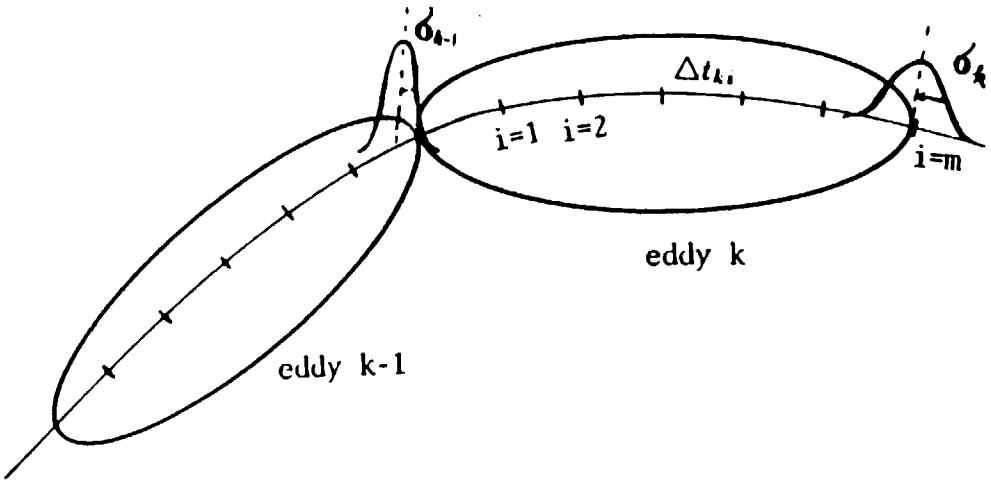

Figure 2.1 Eddy interaction with the particles.

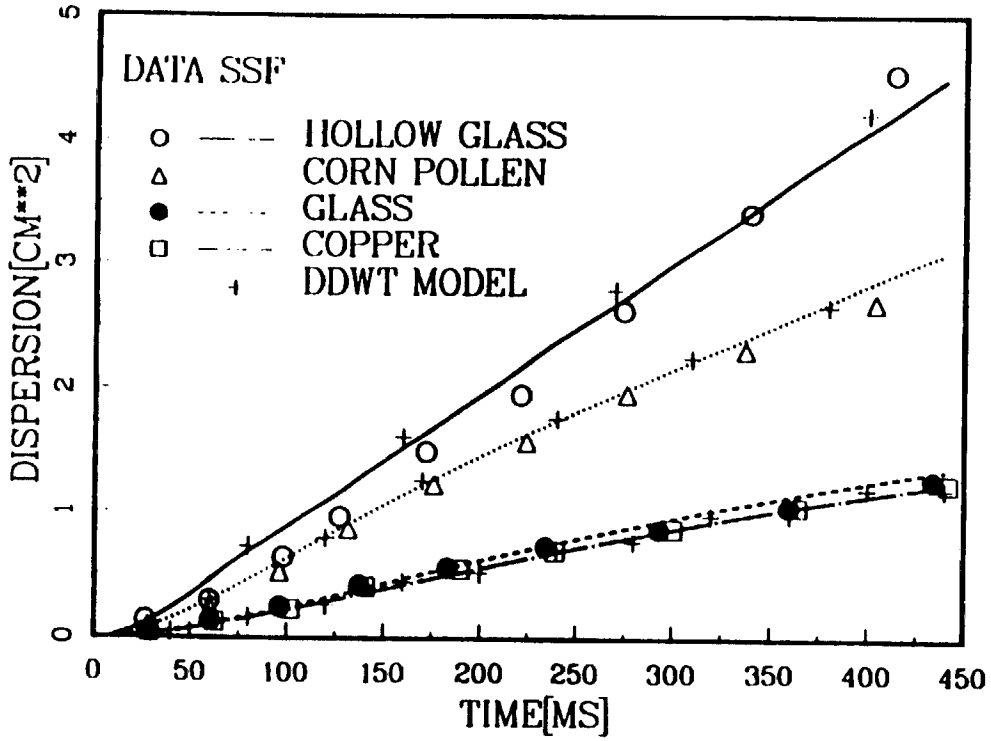

Figure 4.1 Particle dispersion of a nearly-homogeneous flow for SSF model(5000 particles) and DDWT model.

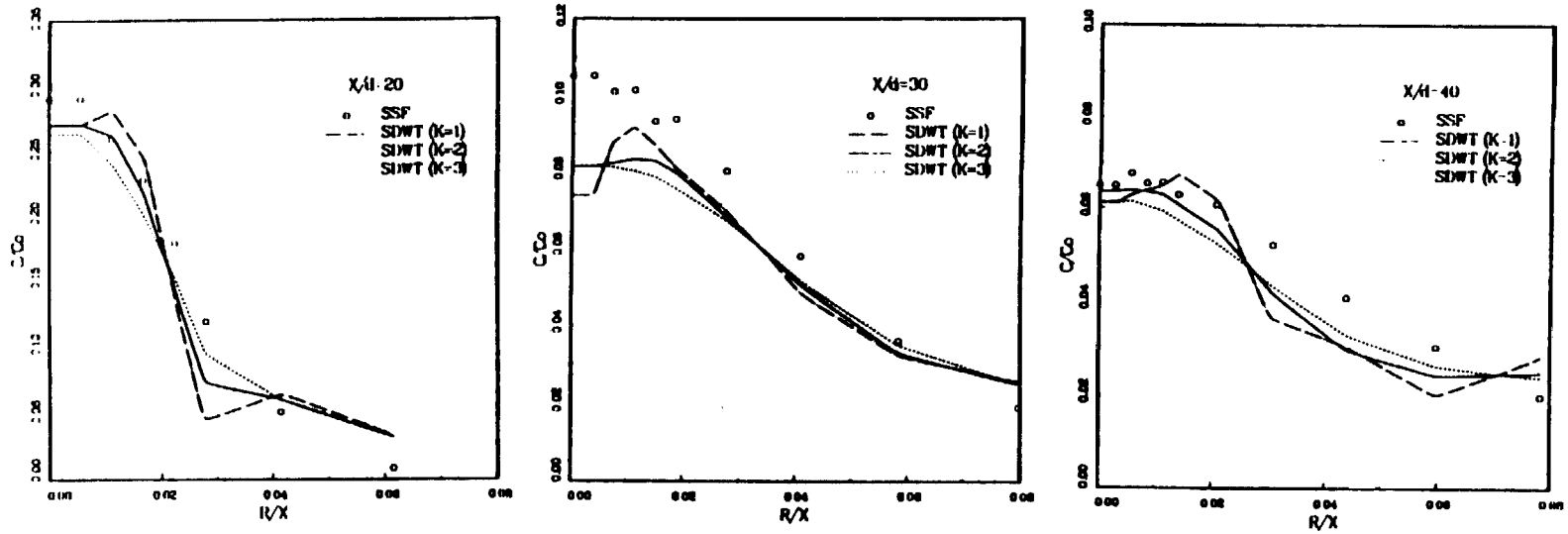

Figure 4.2 Normalized particle concentration distribution of particle laden round jet for SSF model(10,000 particles) and SDWT(50 parcels) with various correction factors.

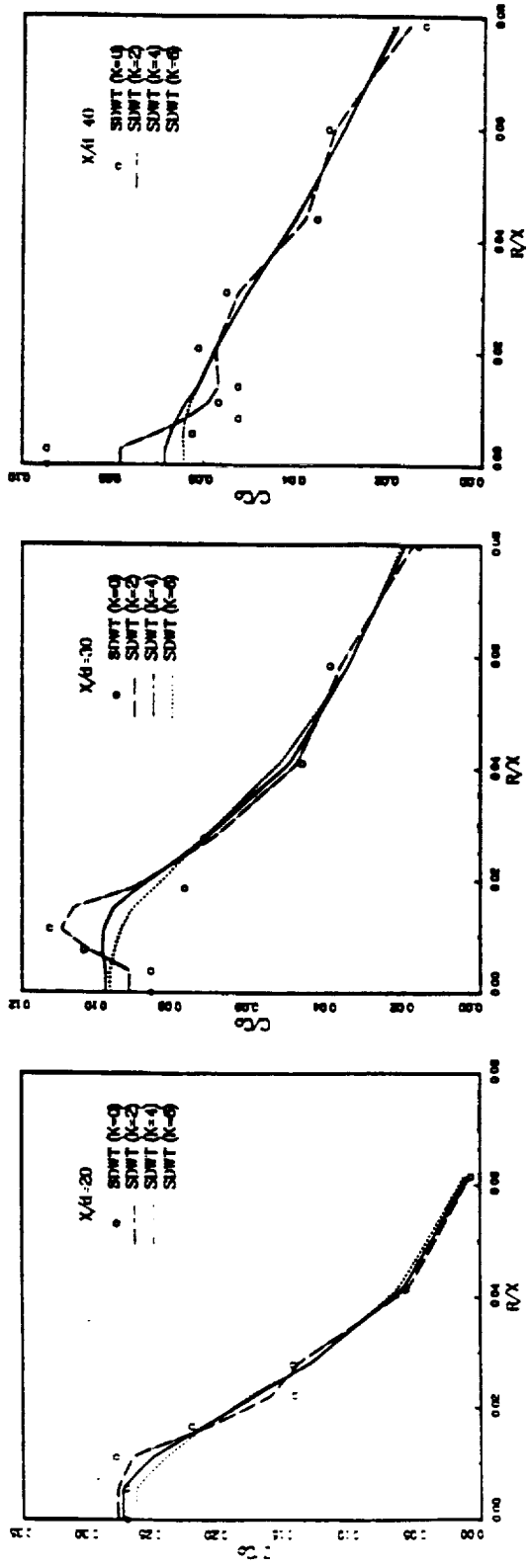

Figure 4.3 Normalized particle concentration distribution of particle laden round jet for SDWT(200 parcels) with various correction factors.

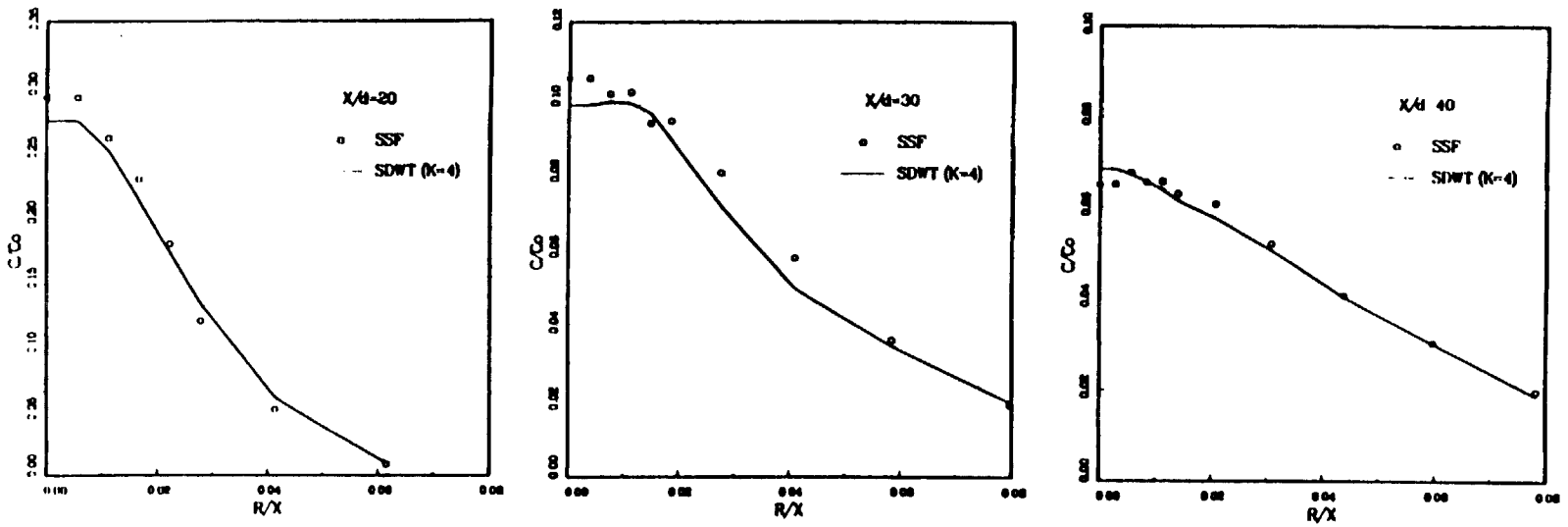

Figure 4.4 Normalized particle concentration distribution of particle laden round jet for SSF model(10,000 particles) and SDWT(200 parcels).

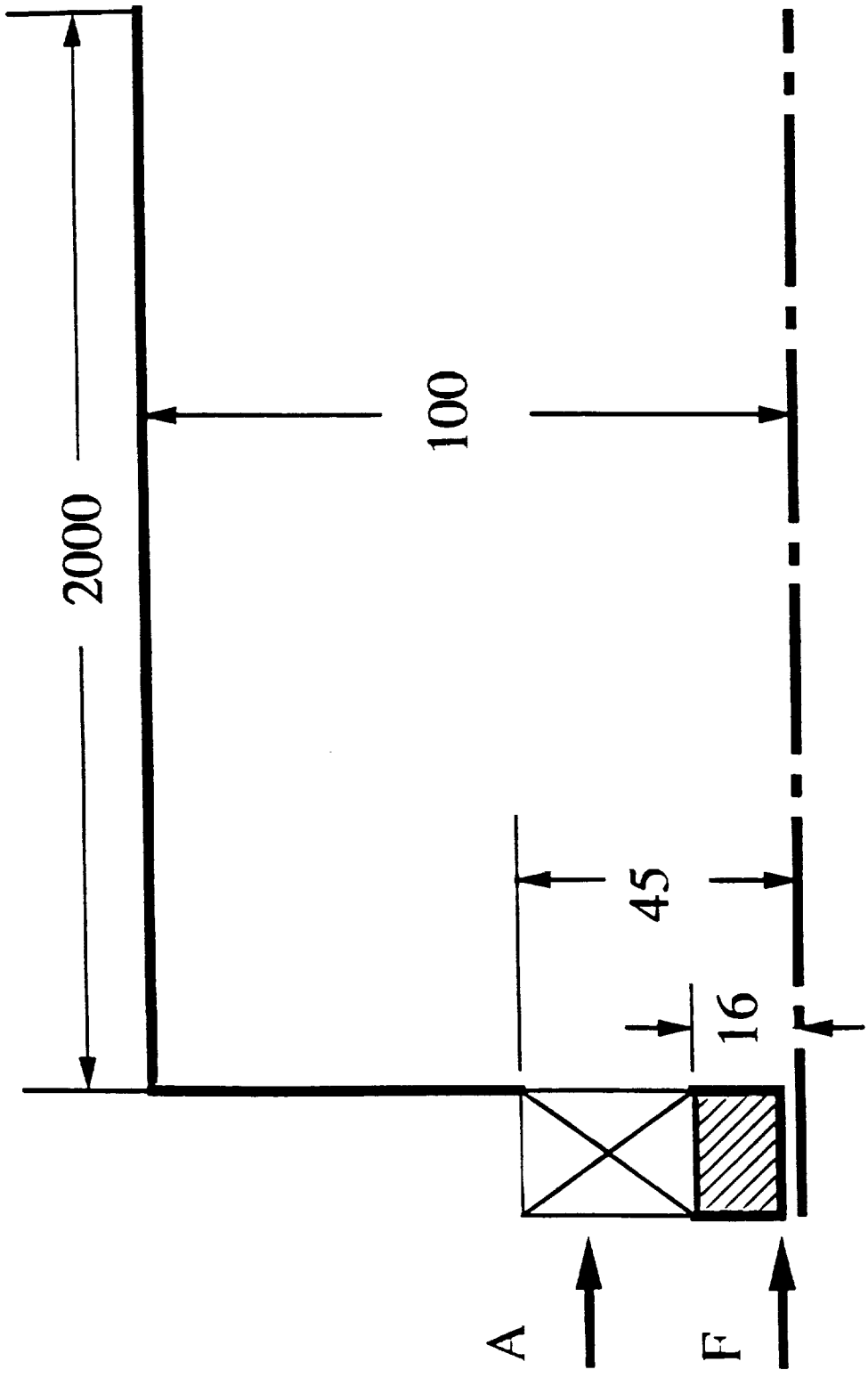

Figure 4.5 Geometry of the hollow-cone spray combustor(Khalil et. al.)

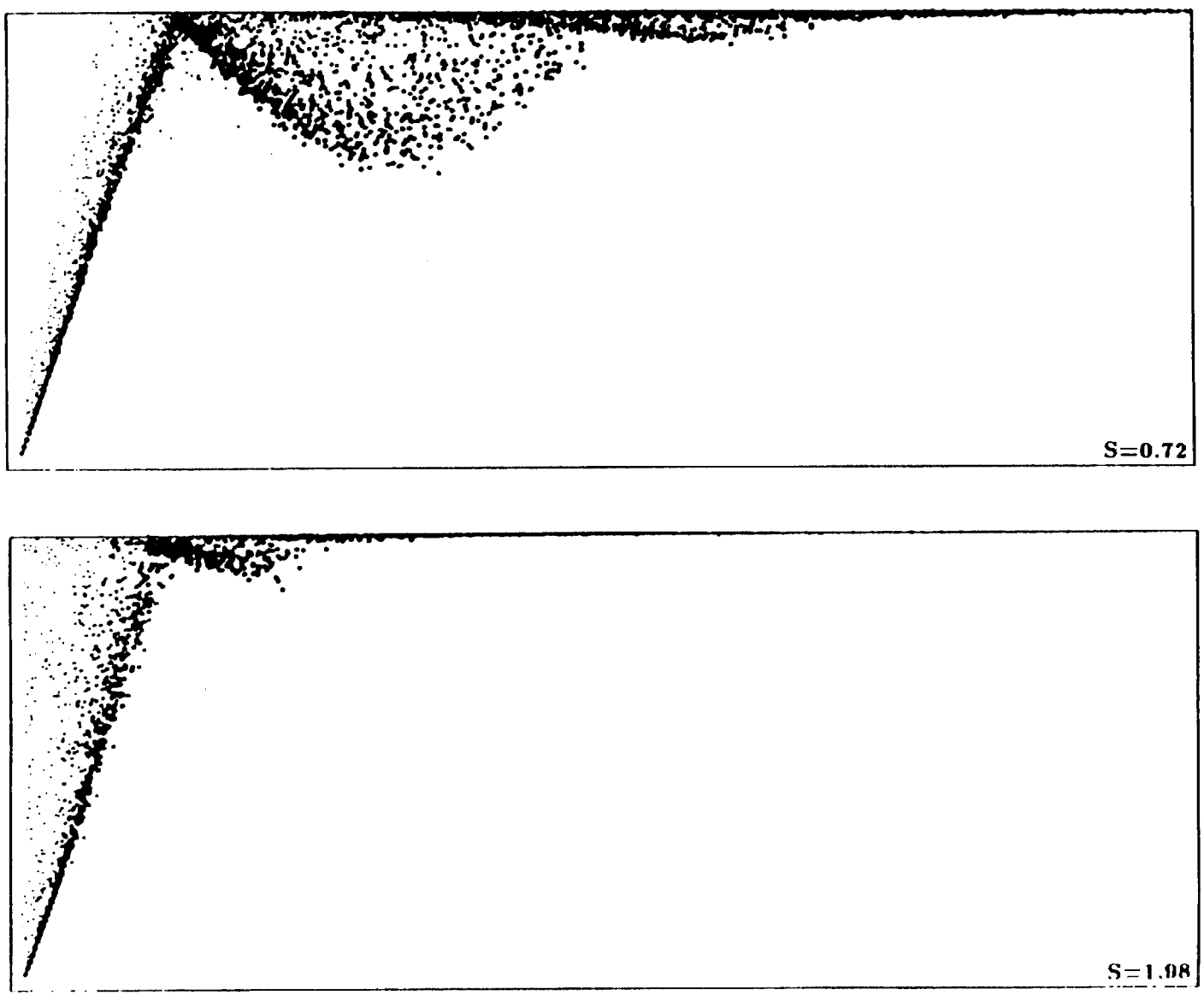

Figure 4.6 Droplet trajectories in kerosene spray flame fields

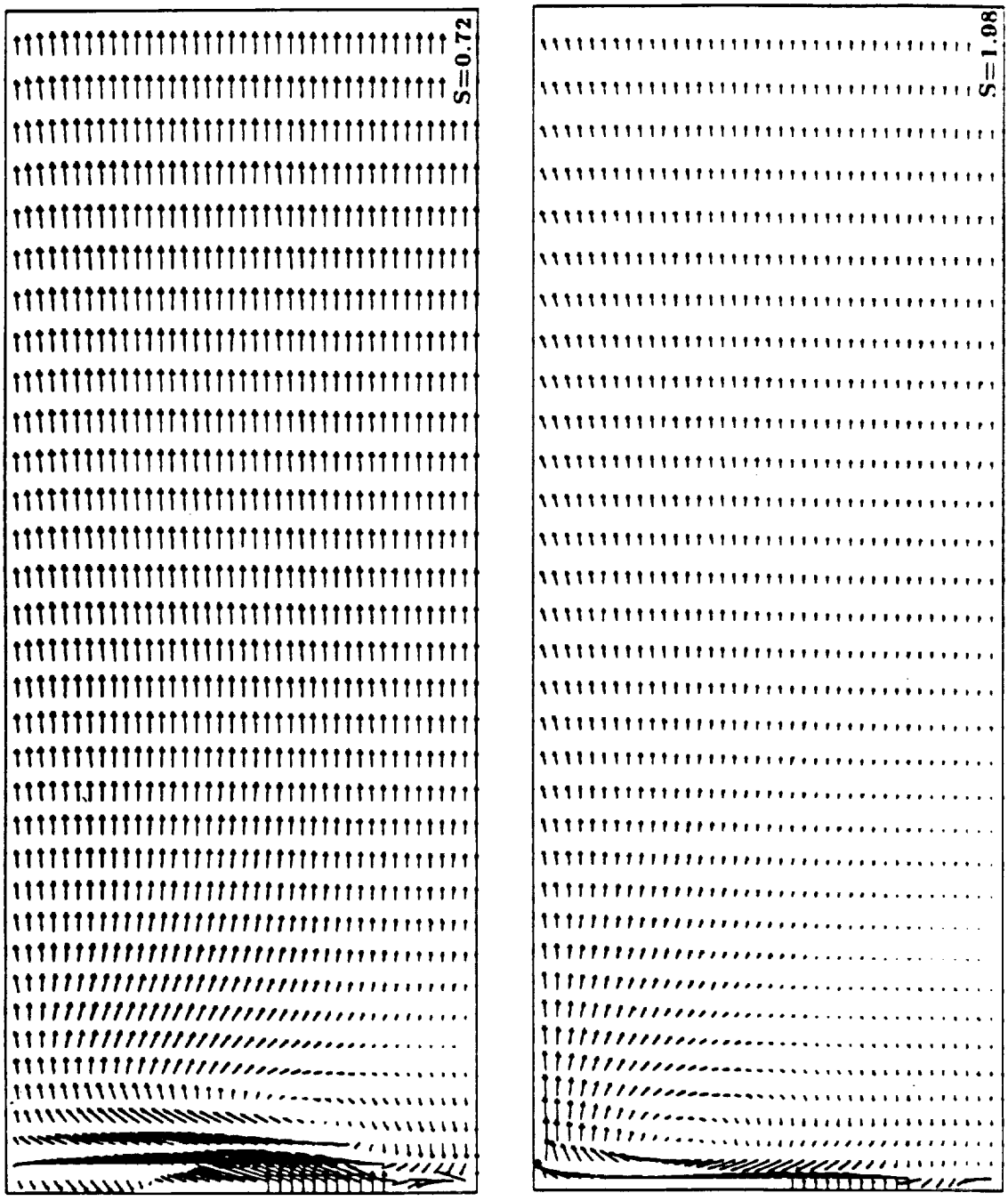

Figure 4.7 Velocity vectors in kerosene spray flame fields

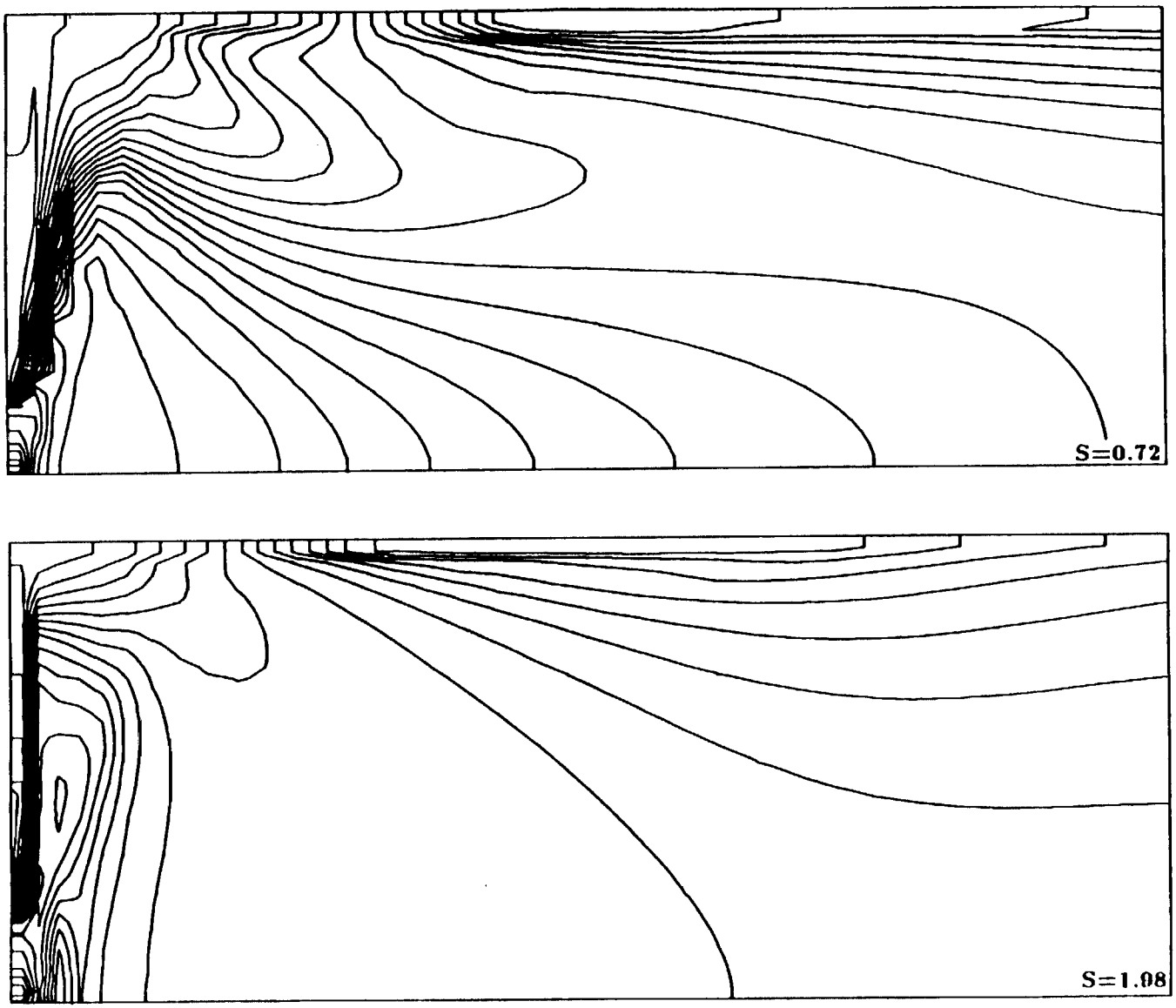

Figure 4.8 Temperature contours in kerosene spray flame fields

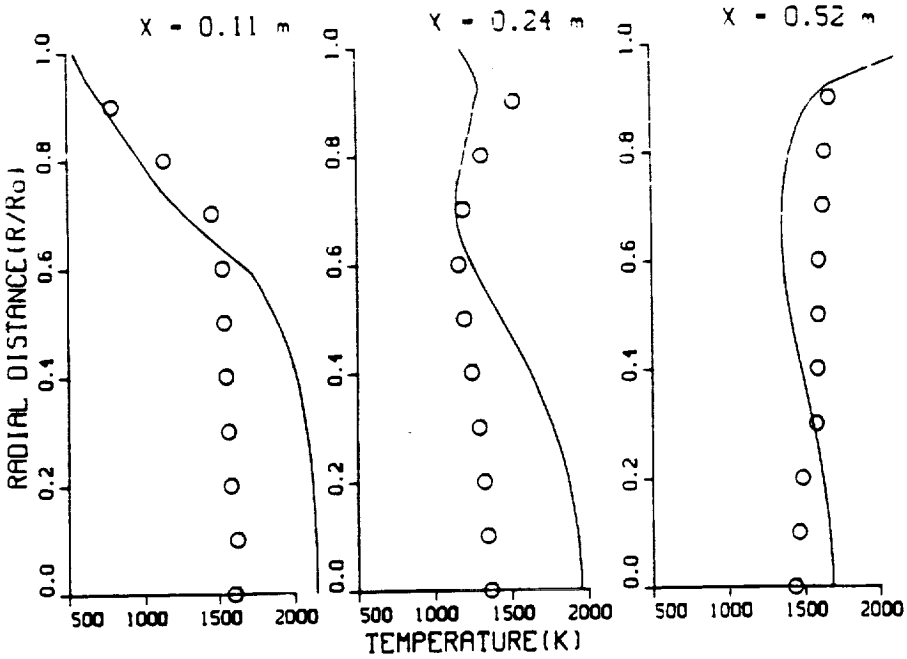

Figure 4.9 Radial profiles of mean temperature(S=0.72)

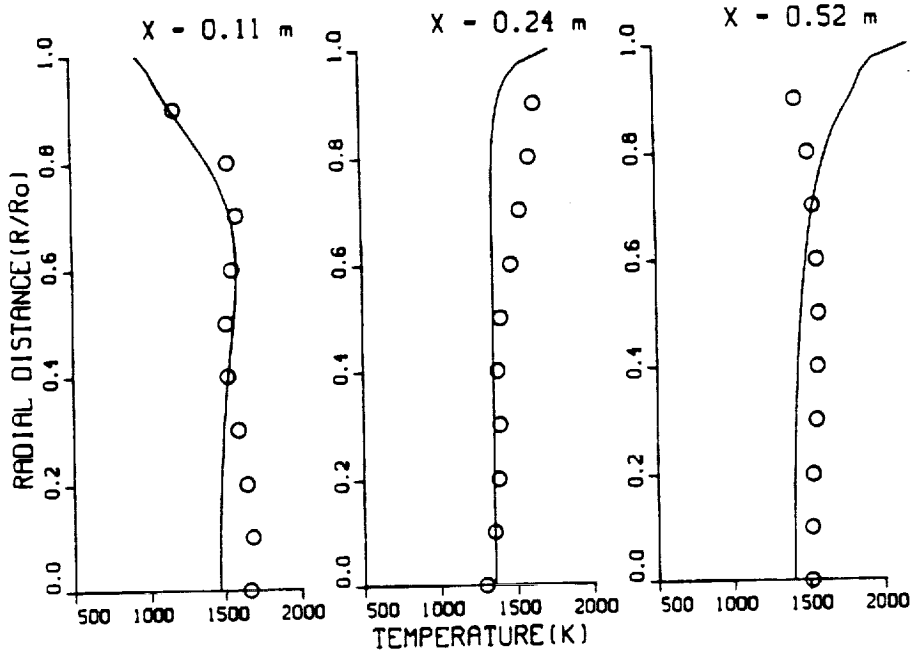

Figure 4.10 Radial profiles of mean temperature(S=1.98)

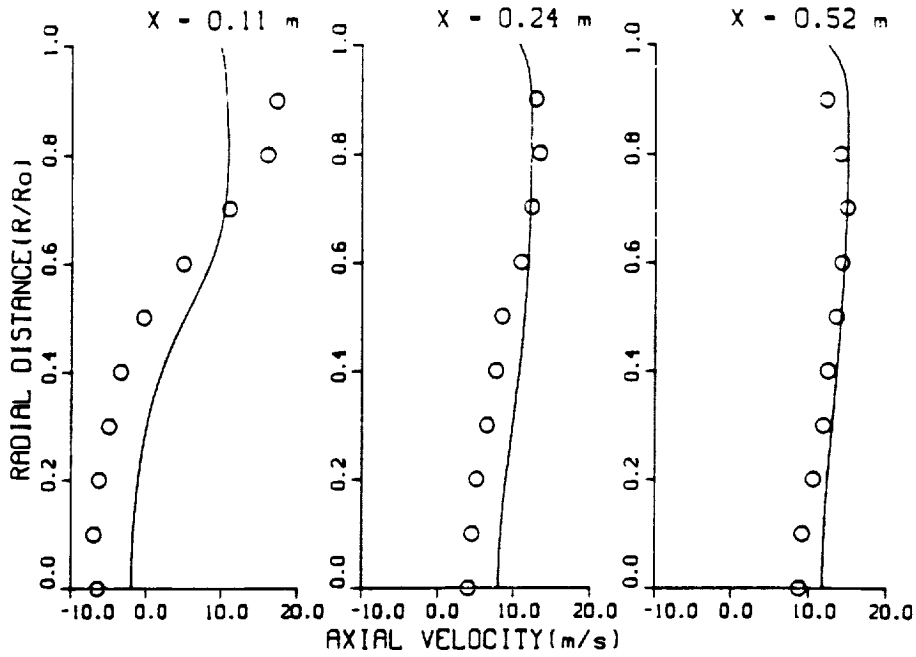

Figure 4.11 Radial profiles of mean axial velocity(S=0.72)

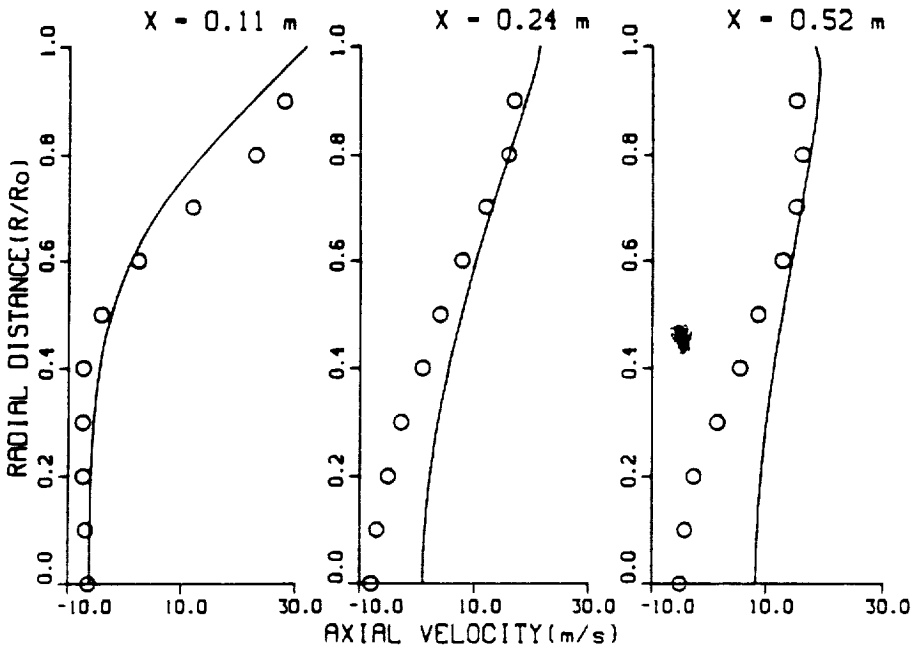

Figure 4.12 Radial profiles of mean axial velocity(S=1.98)

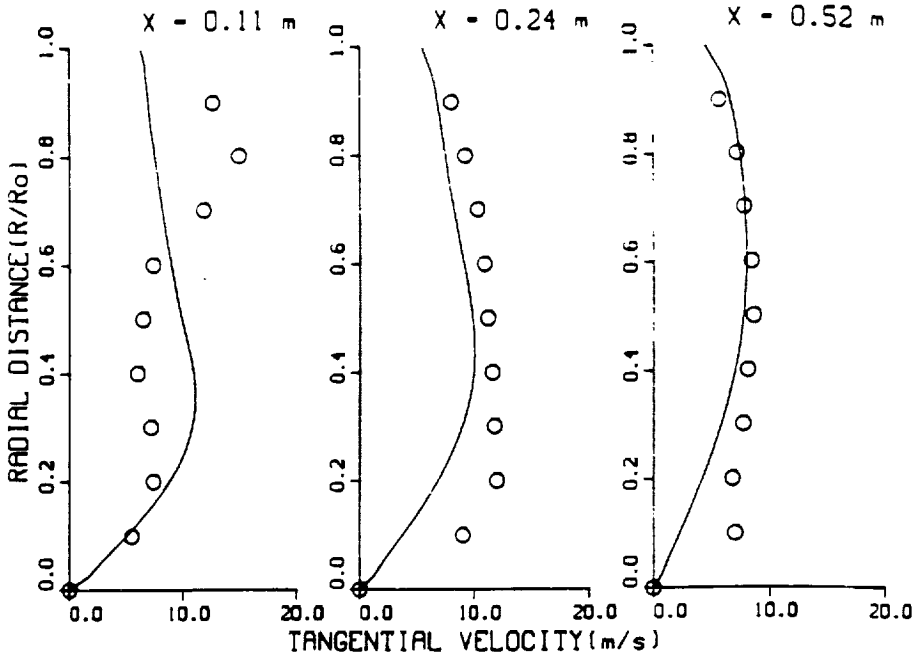

Figure 4.13 Radial profiles of mean tangential velocity(S=0.72)

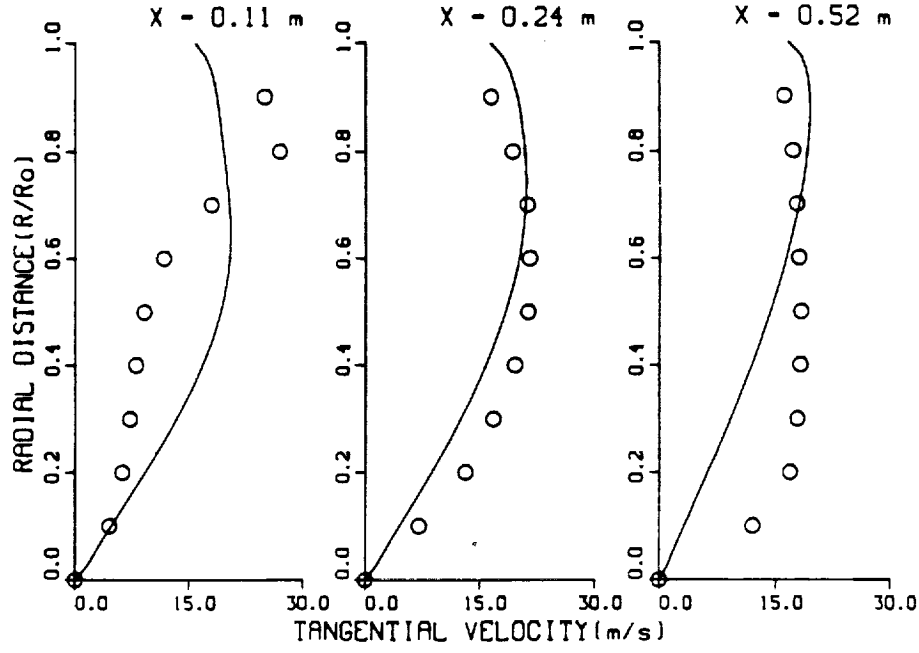

Figure 4.14 Radial profiles of mean tangential velocity(S=1.98)

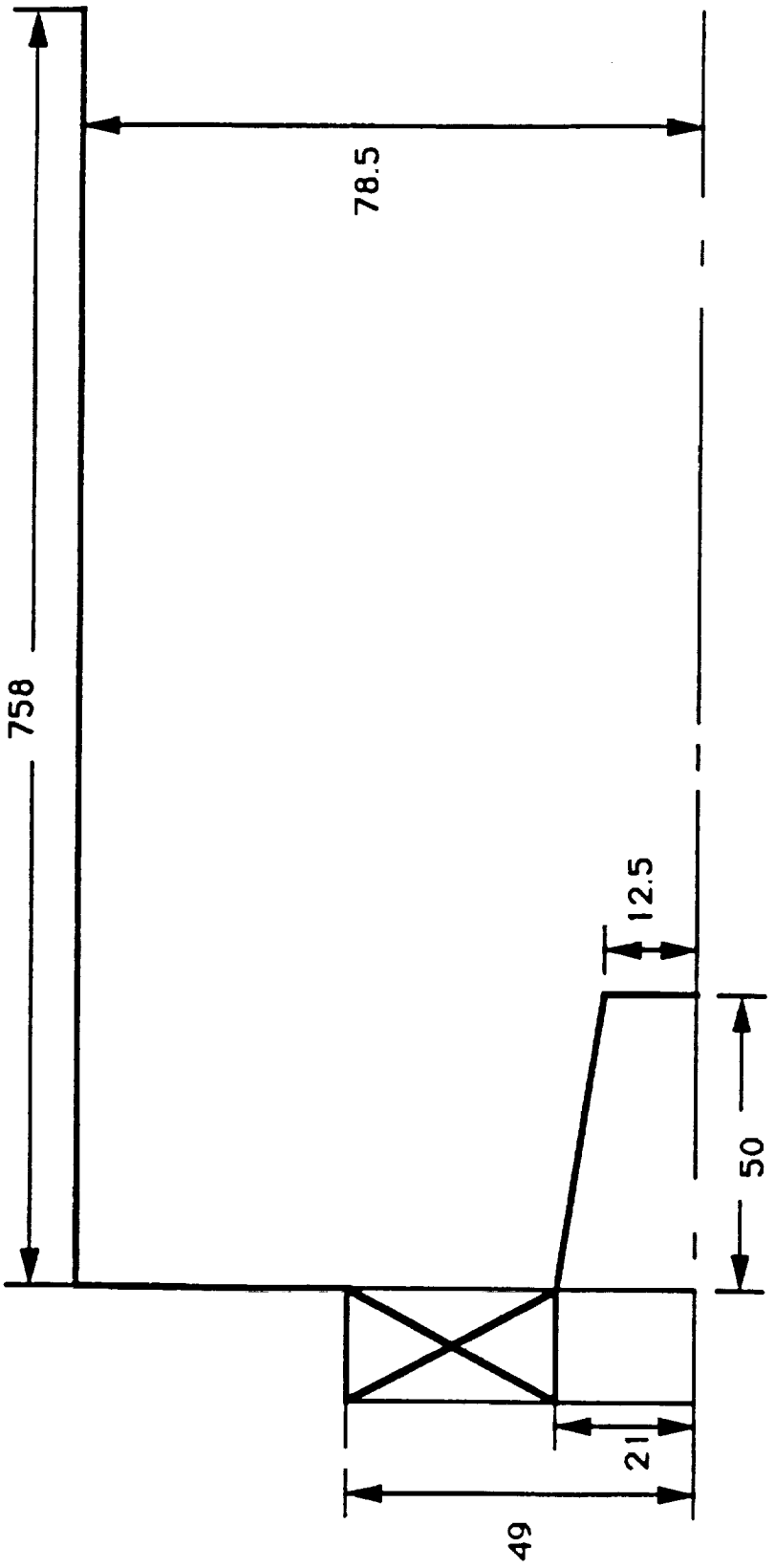

Figure 4.15 Spray combustor with a rotating cup atomizer(El-Banhawy et. al.)

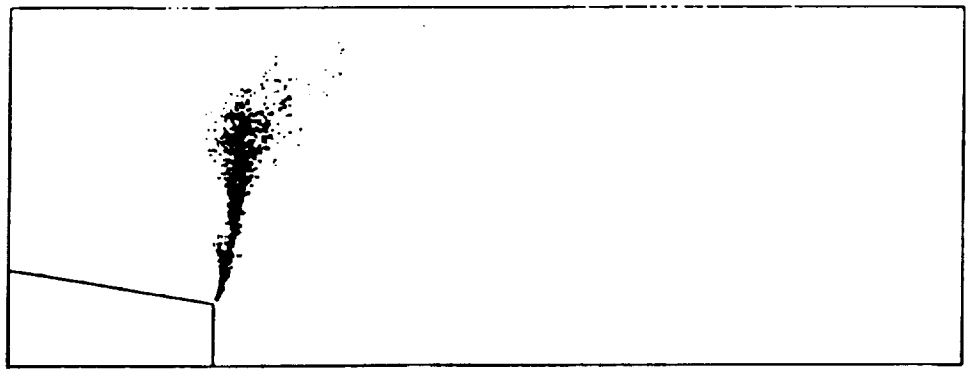

Figure 4.16 Droplet trajectories in kerosene spray flame fields

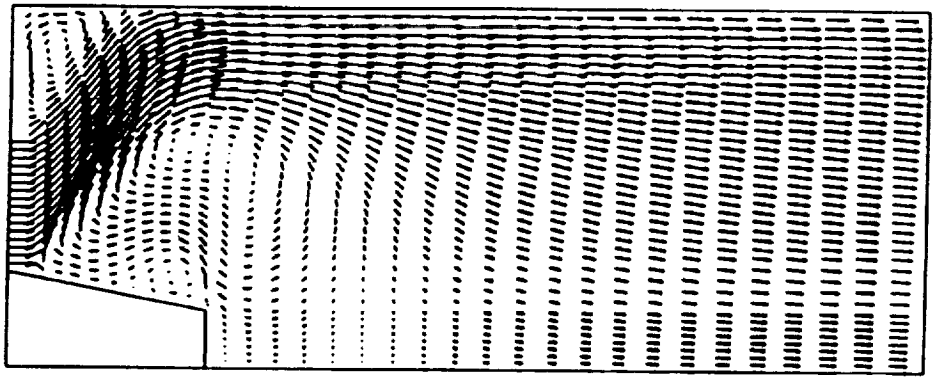

Figure 4.17 Velocity vectors in kerosene spray flame fields

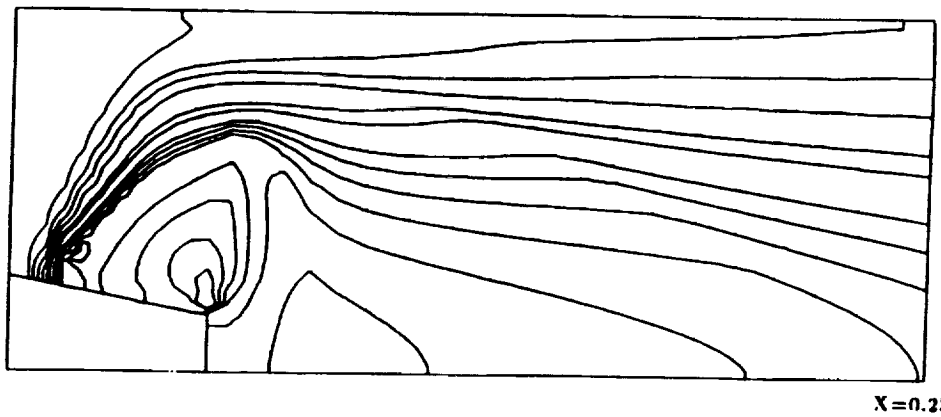

Figure 4.18 Temperature contours in kerosene spray flame fields

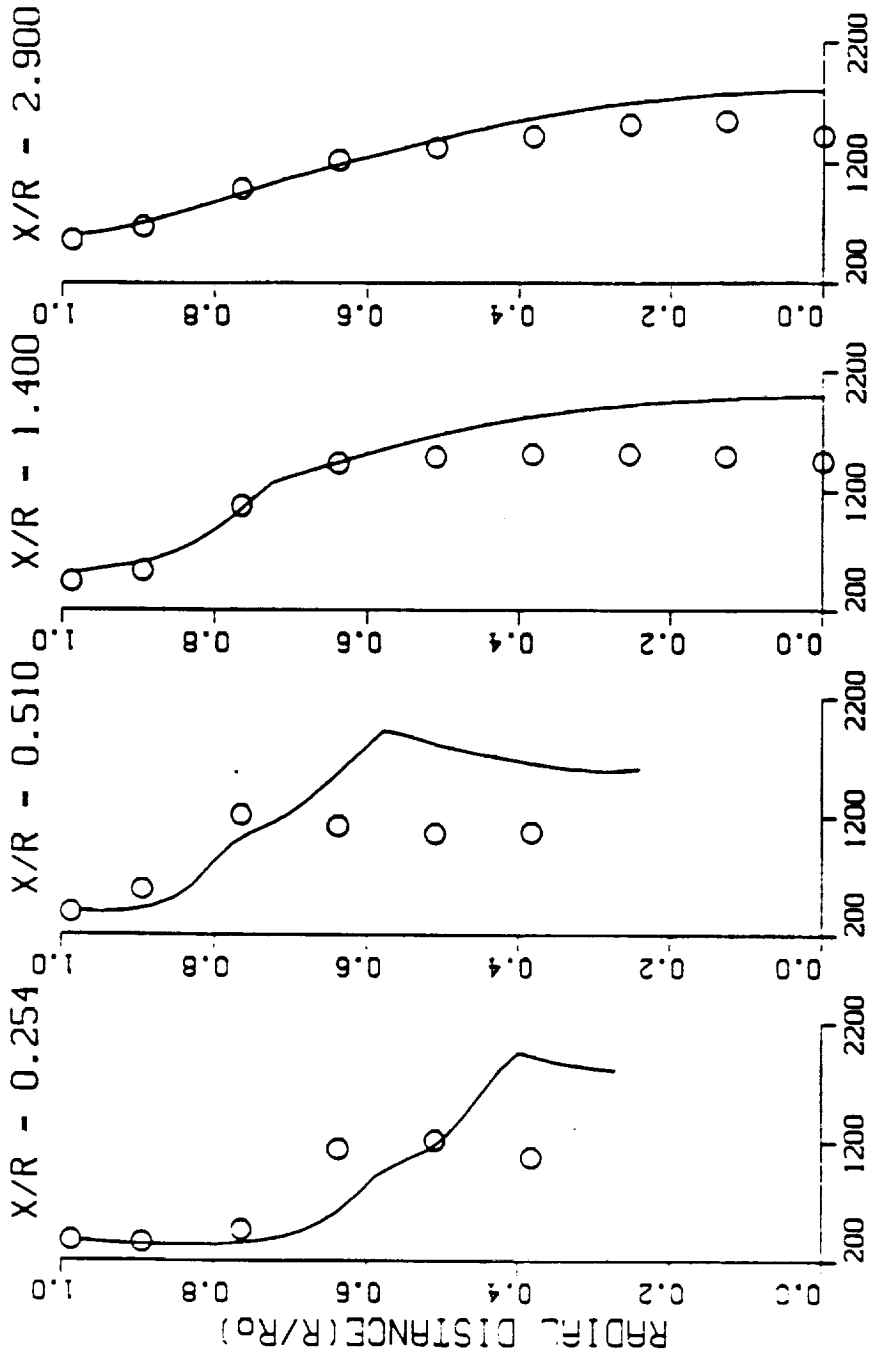

Figure 4.19 Radial profiles of mean temperature(S=1.2)

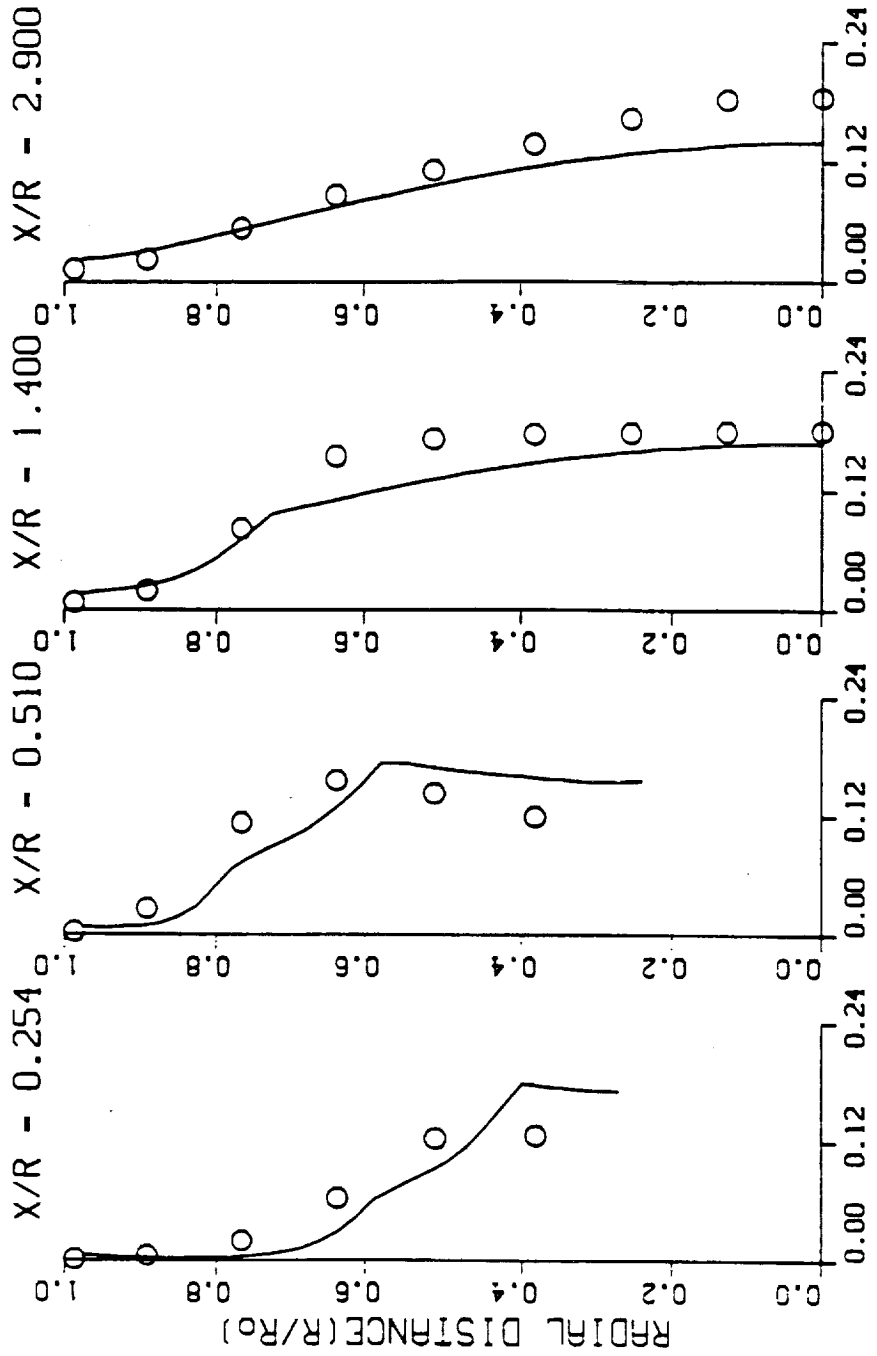

Figure 4.20 Radial profiles of mass fraction of CO_2(S=1.2)

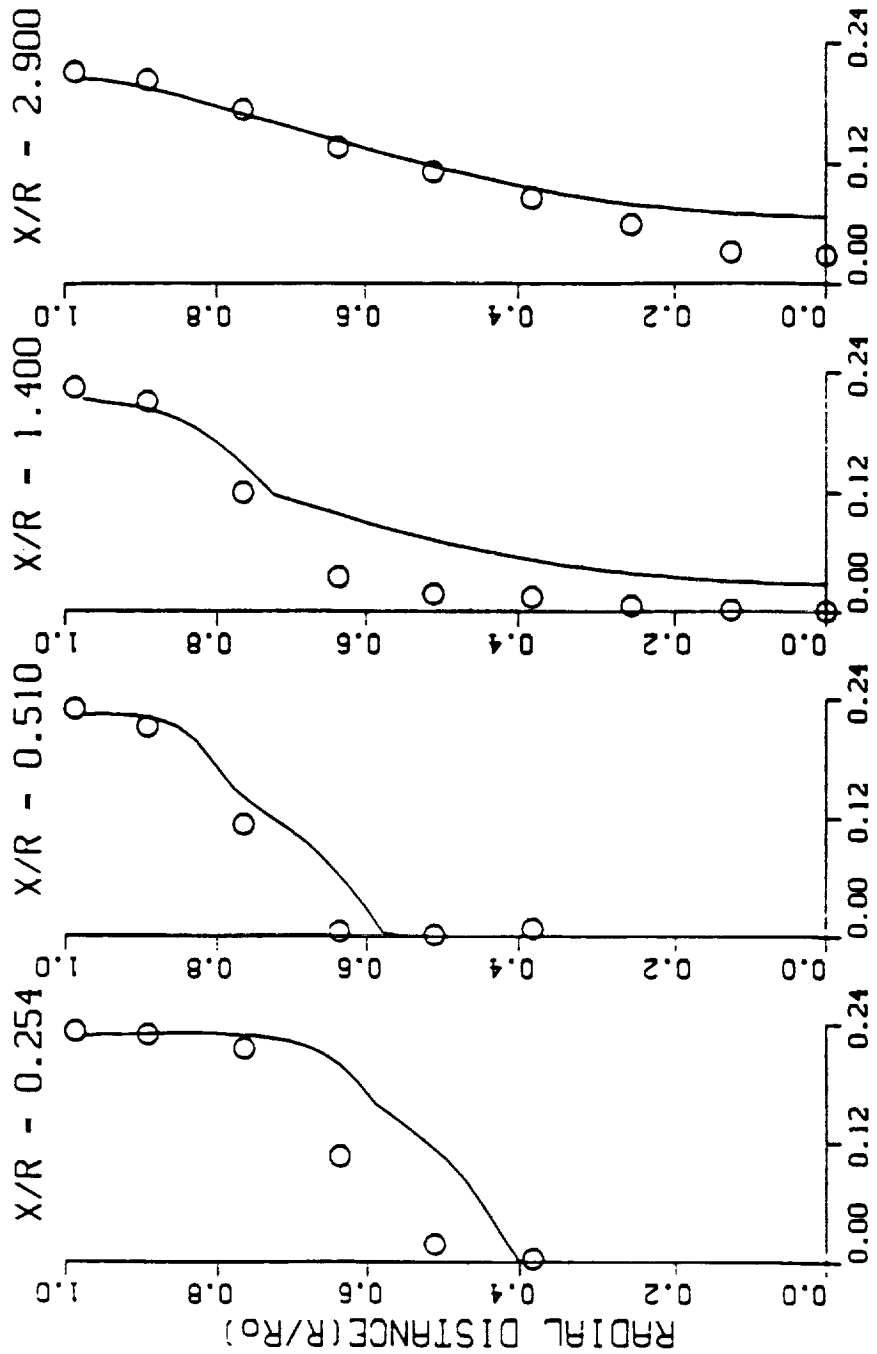

Figure 4.21 Radial profiles of mass fraction of O_2(S=1.2)

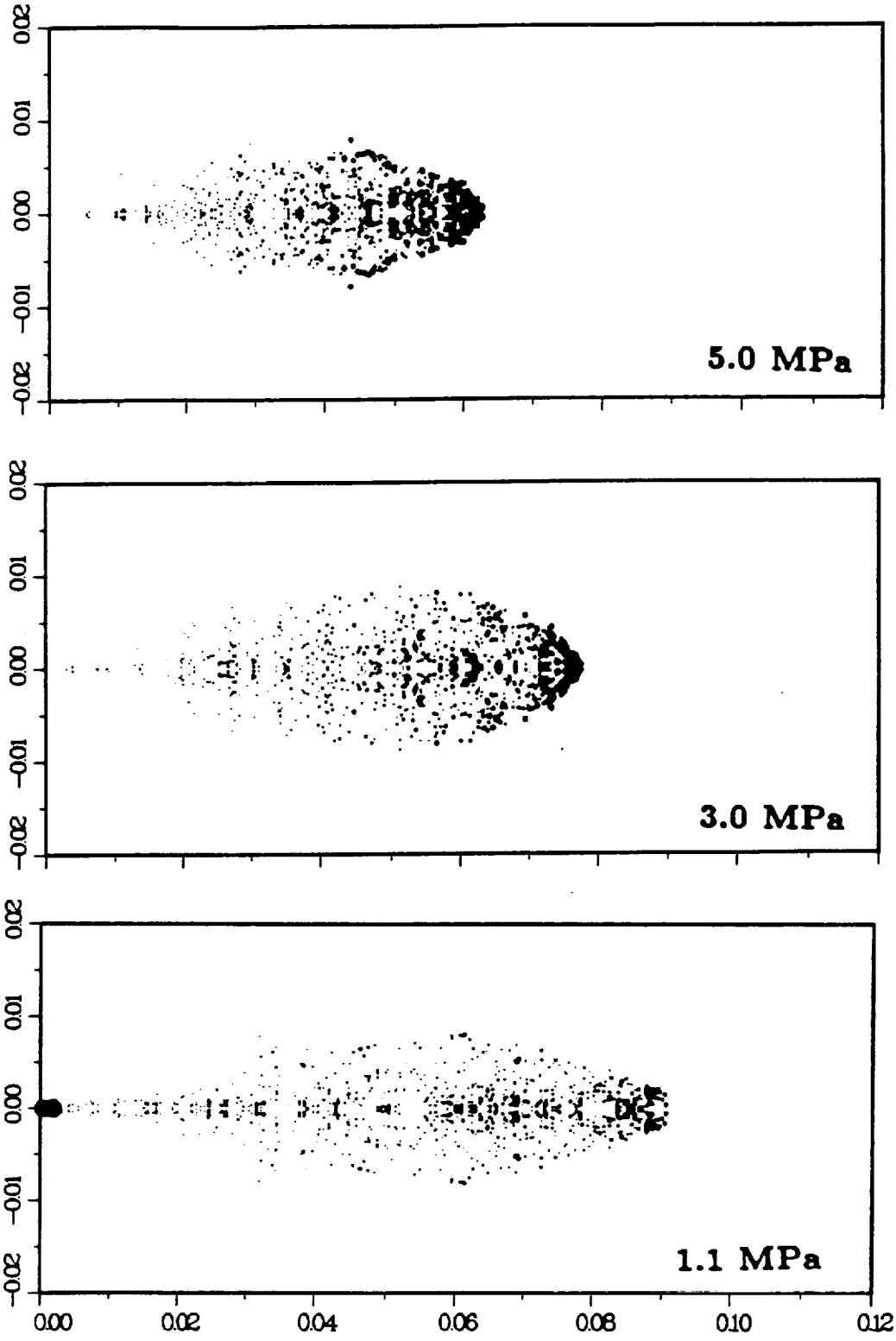

Figure 4.22 Spray parcel distribution in a solid-cone spray($t = 3.0ms$)

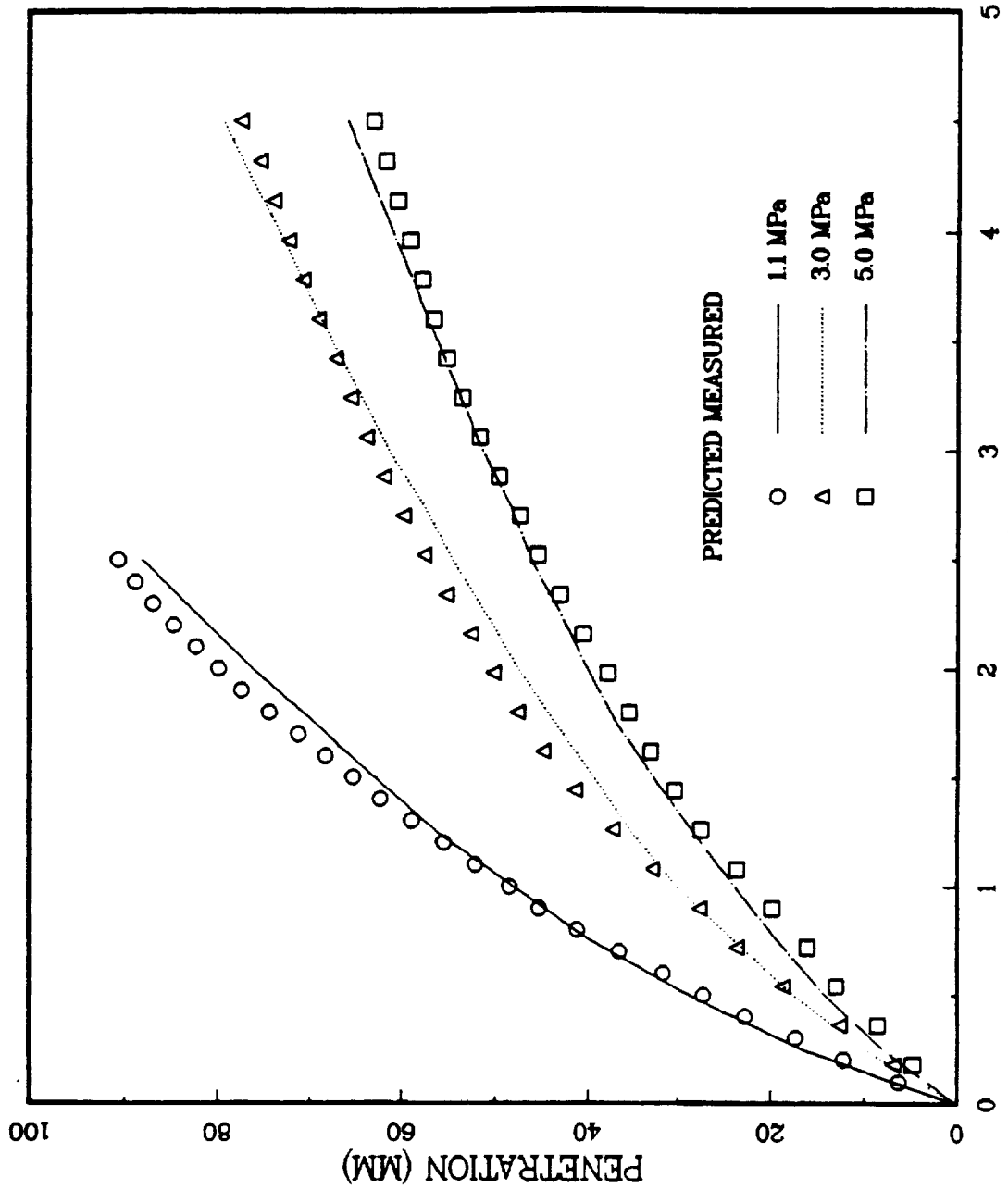

Figure 4.23 Spray tip penetration versus time in a solid-cone spray

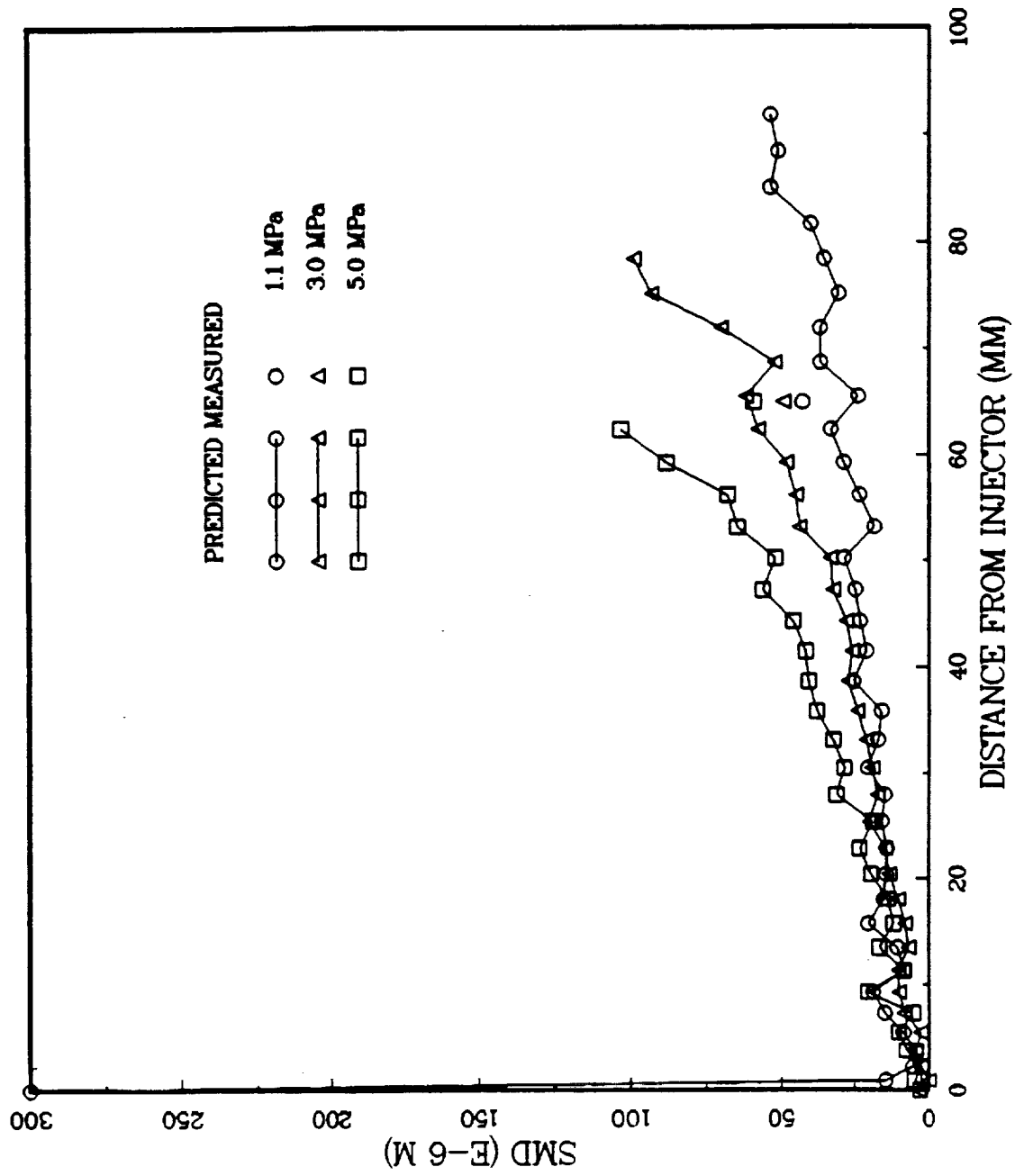

Figure 4.24 Sauter mean diameter versus distance from the injector

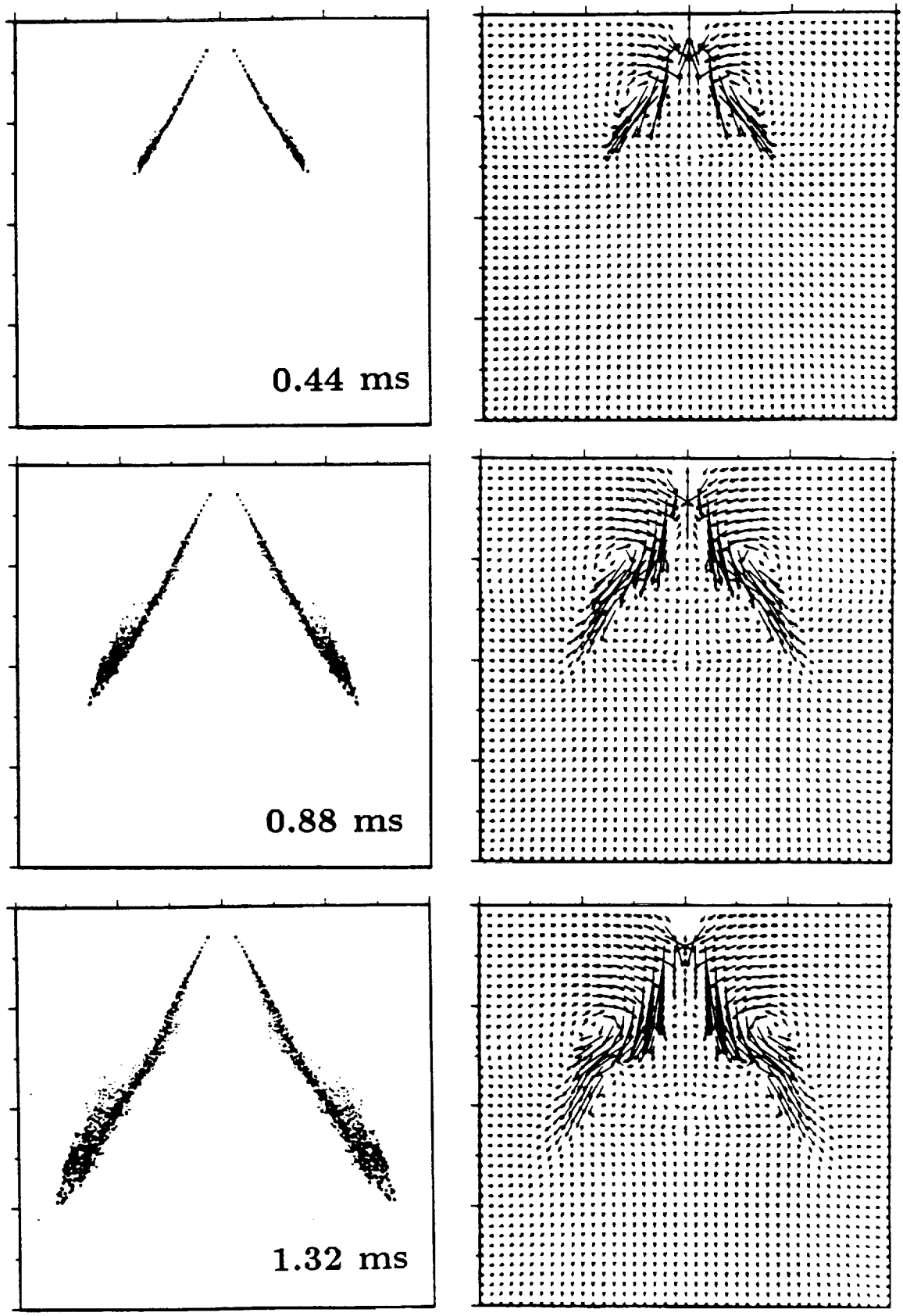

Figure 4.25 Spray parcel distribution and velocity vectors in a hollow-cone spray

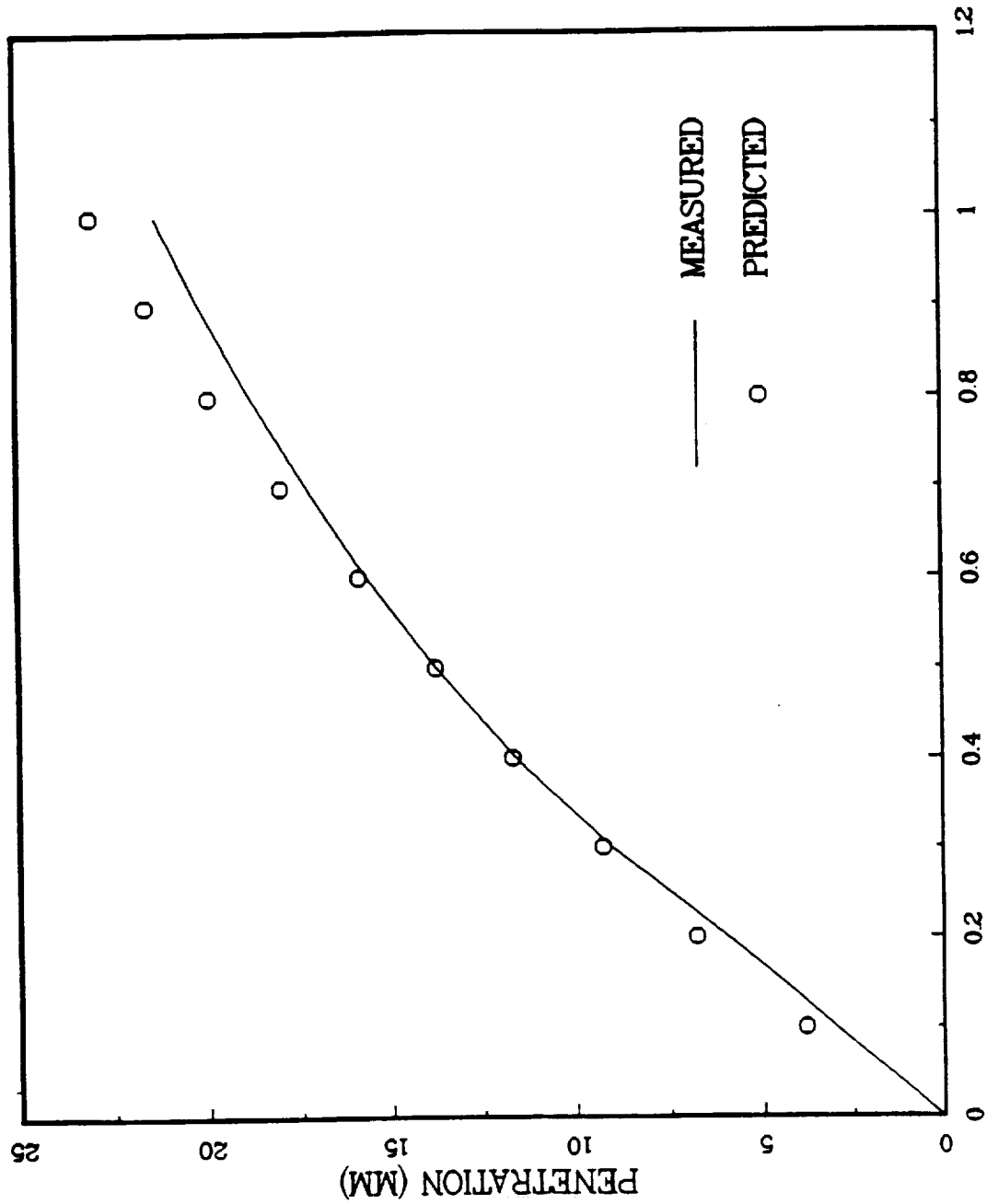

Figure 4.26 Spray tip penetration versus time in a hollow-cone spray

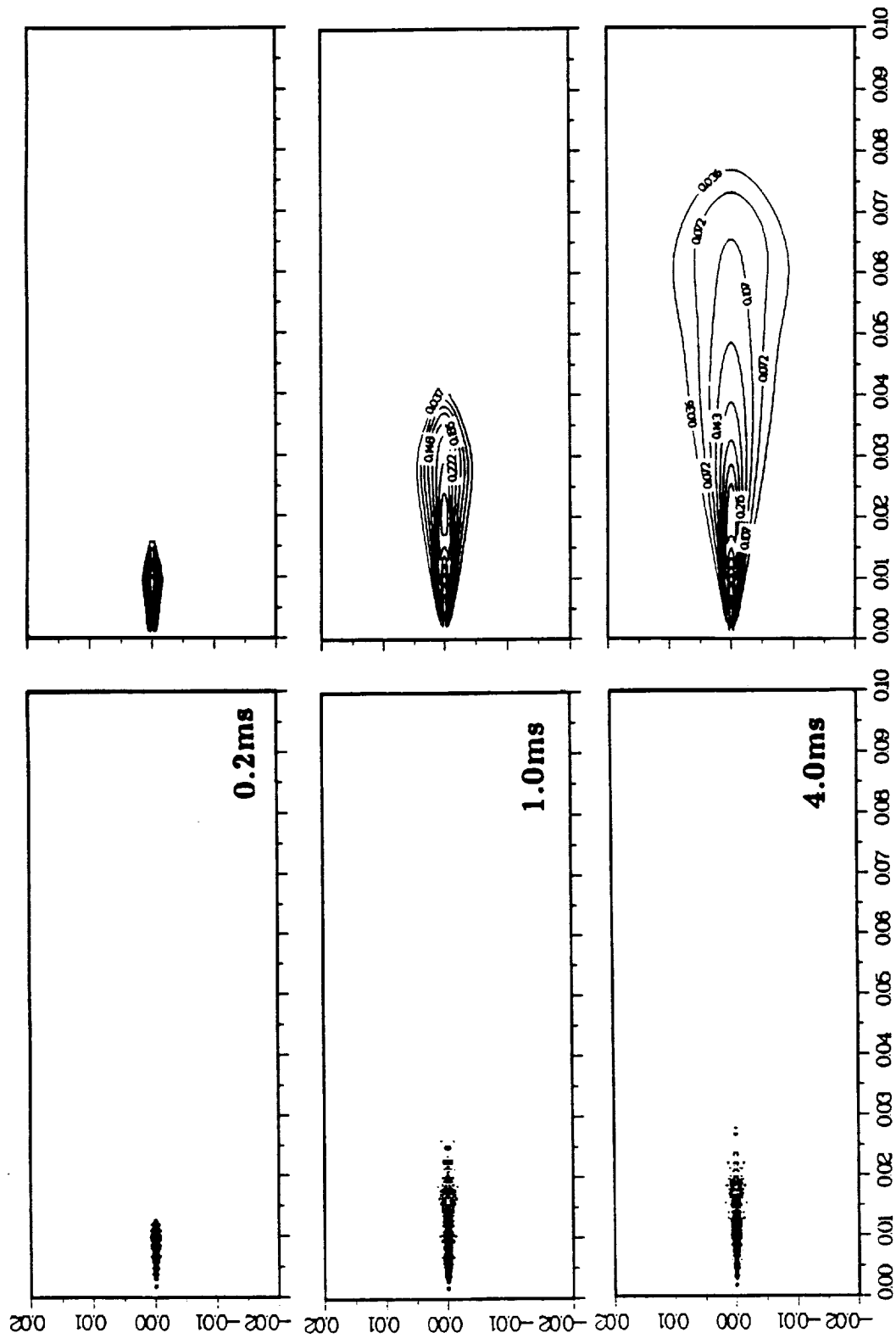

Figure 4.27 Spray parcel distribution and contours of fuel mass fraction in an evaporating spray

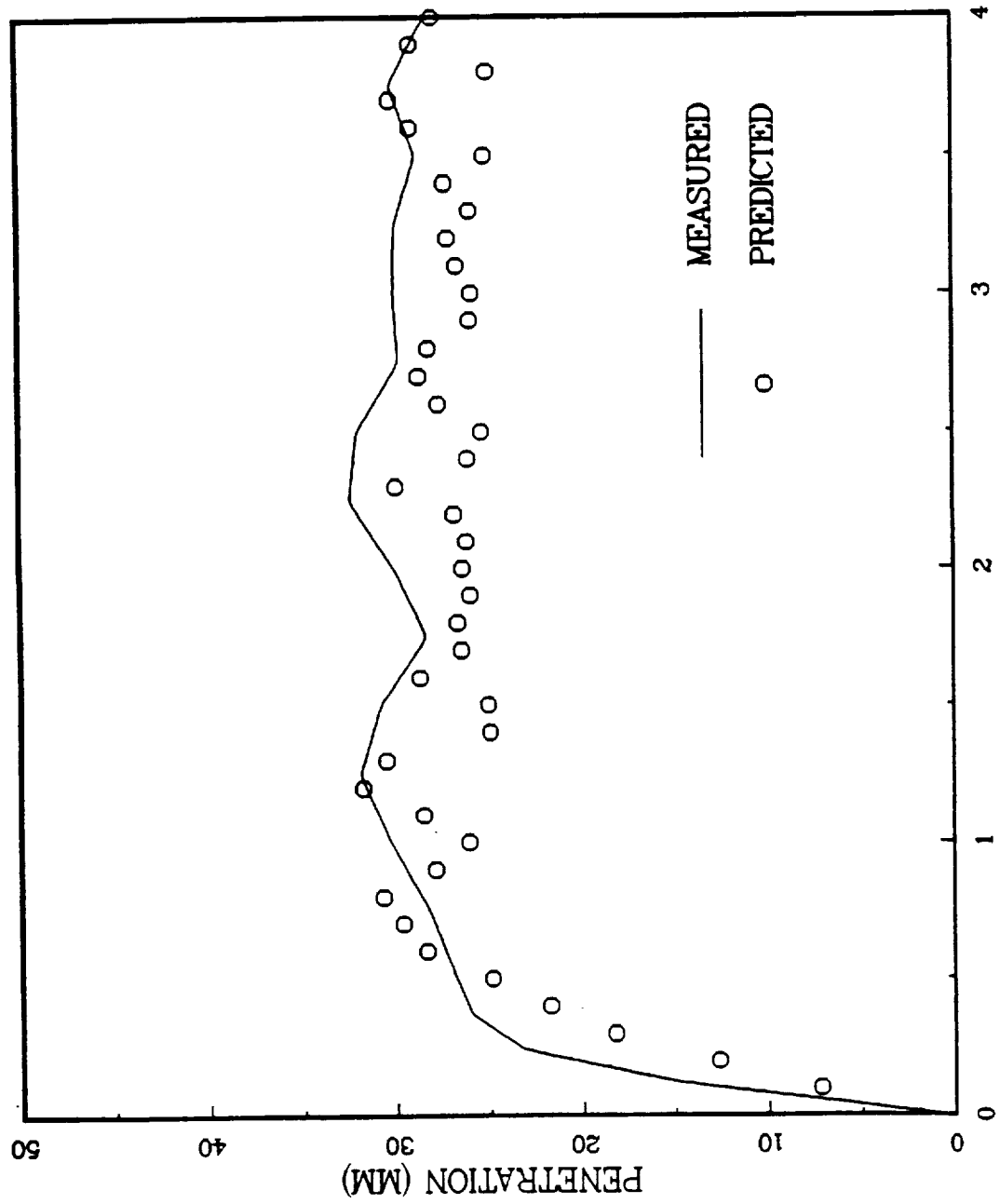

Figure 4.28 Spray tip penetration versus time in an evaporating spray

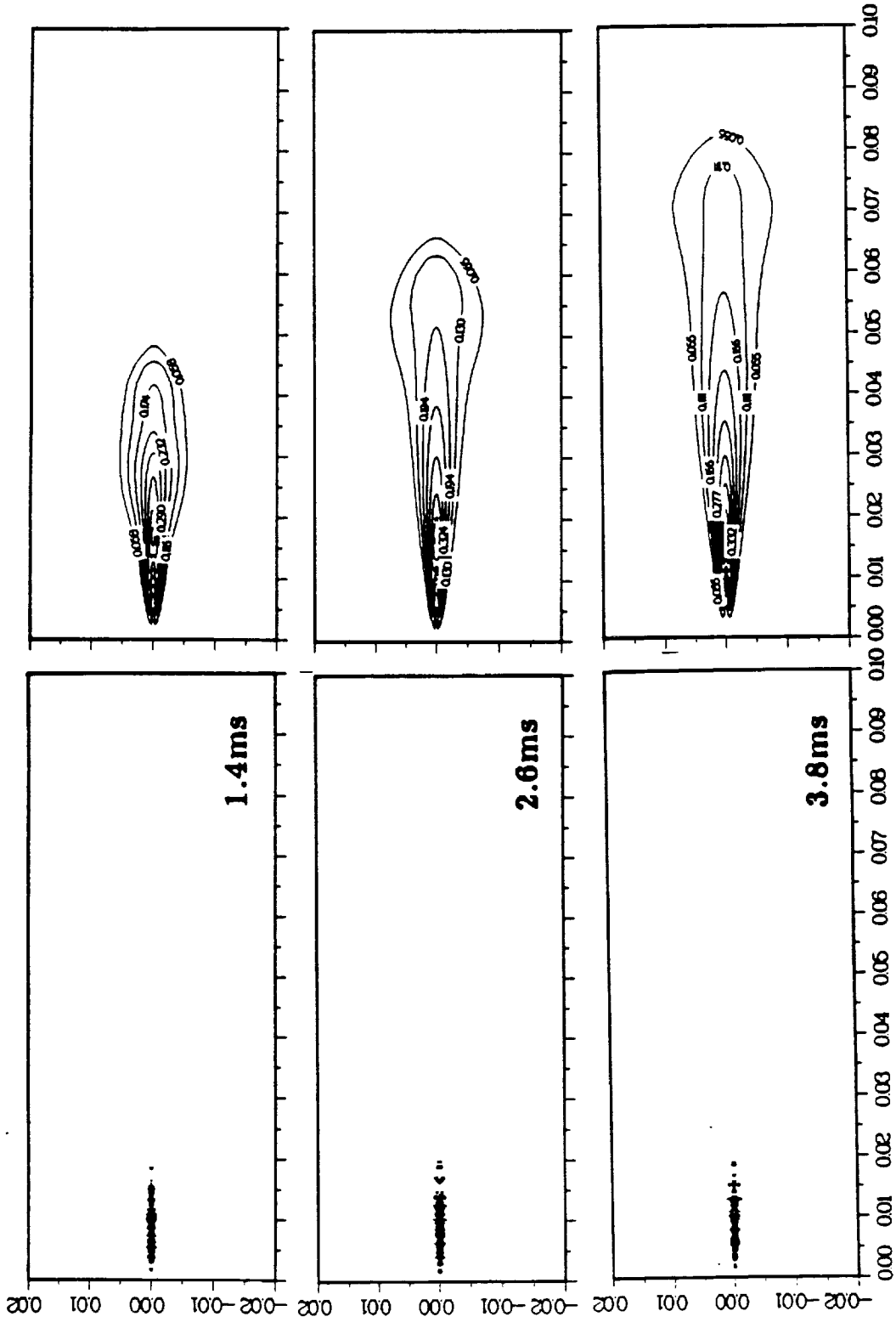

Figure 4.29 Spray parcel distribution and contours of fuel mass fraction in a burning spray

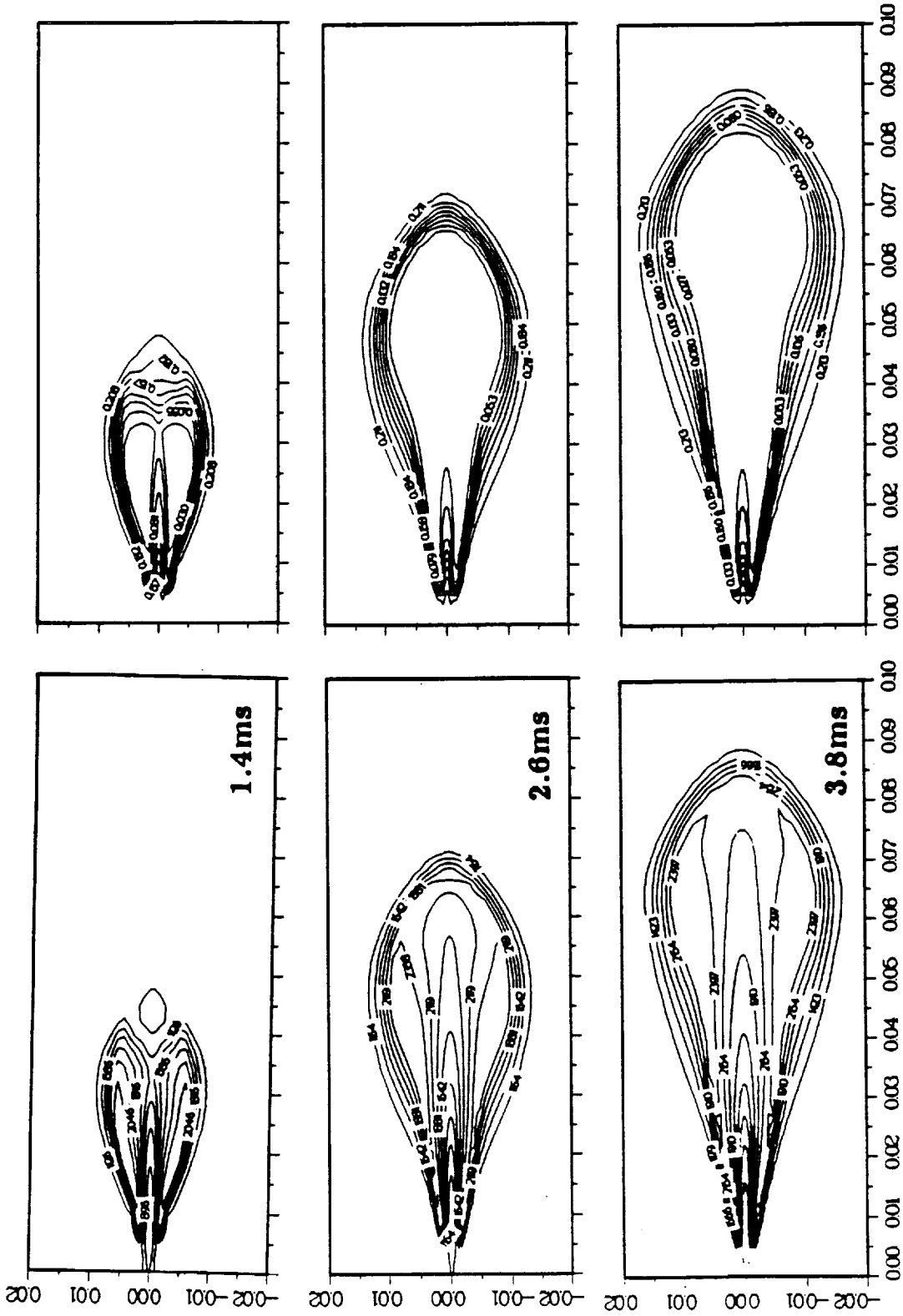

Figure 4.30 Contours of temperature and oxygen mass fraction in a burning spray

APPENDIX A. Two-Phase Interaction Source Terms

The two-phase interaction source terms in the governing equations can be expressed as :

$$S_{m,l} = \sum_{p=1}^{NP} N_p m_{ev,p}/dV \tag{A.1}$$

$$S_{ui,l} = \sum_{p=1}^{NP} [N_p m_{ev,p}(v_i)_p - \frac{4}{3}\pi\rho_d {r_p}^3 N_p (\frac{dv_i}{dt})_p]/dV \tag{A.2}$$

$$S_{h,l} = \sum_{p=1}^{NP} \{N_p m_{ev,p}(h_p - L + \frac{1}{2}v_i^2)$$

$$-\frac{4}{3}\pi\rho_d {r_p}^3 N_p[(C_{p,d}\frac{dT_p}{dt} + (\frac{dv_i}{dt}(v_i - u_i)_p)]\}/dV \tag{A.4}$$

where

$$(\frac{dv_i}{dt})_p = \frac{u_i^{n+1} + u_i' - v_i^{n+1}}{\tau} + F_{bi} \tag{A.4}$$

Here, dV denotes the volume of the computational cell and h_p and L are the droplet enthalpy and the latent heat of the droplet, respectively.

To improve the covergence and the numerical stability, the momentum interaction source term, $S_{ui,l}$ can be treated implicitly.

$$S_{ui,l}^{n+1} = -S_u u_i^{n+1} + R_u \tag{A.5}$$

Here, S_u and R_u are obtained by substituting (A.4) into (A.2):

$$S_u = \frac{1}{dV}\sum_{p}^{NP} N_p m_p/(\Delta t + \tau_p) \tag{A.6}$$

$$R_u = \frac{1}{dV}\sum_{p}^{NP} N_p m_p/(\Delta t + \tau_p)(v_i^n - u_i' + F_{bi}\tau_p) \tag{A.7}$$

and $m_p = \frac{4}{3}\pi r_p^3 \rho_d$ is the particle mass. The parameters S_u and R_u are momentum control volume quantities depending on available particle information at previous timestep.

APPENDIX B. Numerics of Beta Probability Density Function

The density-weighted mean mixture properties ($\overline{\phi}_m$) at any location evaluated by convoluting the property functions with a probability density function, $P(\xi, x_i)$:

$$\overline{\phi}_m(x_i) = \int_0^1 \phi_m(\xi) P(\xi, x_i) d\xi \qquad (B1)$$

where

$$P(\xi, x_i) = \frac{\xi^{a-1}(1-\xi)^{b-1}}{\int_0^1 \xi^{a-1}(1-\xi)^{b-1} d\xi} \qquad (B2)$$

The denomenator in Eq.(B2) is the Beta function, $B(a,b)$. Note that $B(a,b)$ can be calculated from the Gamma function, Γ with the aid of the following relationship:

$$B(a,b) = \frac{\Gamma(a)\Gamma(b)}{\Gamma(a+b)} \qquad (B3)$$

Substituting Eq.(B2) into Eq.(B1) yields

$$\overline{\phi}_m(x_i) = \frac{1}{B(a,b)} \int_0^1 \phi_m(\xi) \xi^{a-1}(1-\xi)^{b-1} d\xi \qquad (B4)$$

The numerator of Eq.(B5) can be integrated by a trapzoidal rule or Gaussian quadrature. However, the significant errors can be produced unless the increments in ξ are chosen to be quite small. These numerical errors are due to the spikey nature of the Beta pdf when the variance (g) of the mixture fraction is small and also when the mean mixture fraction(f) is close to 0 or 1. To avoid this problem, $\phi_m(\xi)$ is expressed as polynomials of the conserved scalar(ξ). To keep the function monotonic, the integration domain ($0 \leq \xi \leq 1$) is split into two sections: 0 to ξ_s and ξ_s to 1, where ξ_s is the stoichiometric value. The property ϕ_m is expressed as

$$\phi_m(\xi) = \sum_n c_{mn} \xi^n \quad when \;\; 0 \leq \xi \leq \xi_s \qquad (B5)$$

$$\phi_m(\xi) = \sum_n d_{mn} \xi^n \quad when \;\; \xi_s \leq \xi \leq 1 \qquad (B6)$$

where

$$m = 1, ..., M \quad (M = index \;\; for \;\; the \;\; property)$$

$$n = 1, ..., N \quad (N = degree\ of\ the\ polynomial)$$

Substituting Eqs.(B5) and (B6) into Eq.(B4) results in

$$\overline{\phi}_m(x_i) = \frac{1}{B(a,b)}[\int_0^{\xi_s} \sum_n c_{mn}\xi^n \xi^{a-1}(1-\xi)^{b-1}d\xi$$

$$+ \int_{\xi_s}^1 \sum_n d_{mn}\xi^n \xi^{a-1}(1-\xi)^{b-1}d\xi] \qquad (B7)$$

where a and b varying with x_i are evaluated from the solutions of the transport equations for f and g. The numerator of Eq.(B7) is simplified as follows:

$$T = \sum_n (c_{mn} - d_{mn}) \int_0^{\xi_s} \xi^{n+a-1}(1-\xi)^{b-1}d\xi$$

$$+ \sum_n d_{mn} \int_0^1 \xi^{n+a-1}(1-\xi)^{b-1}d\xi \qquad (B8)$$

For using IMSL routines, (B8) can be transformed as the convenient expression:

$$T = \sum_n [d_{mn} + (c_{mn} - d_{mn}) \frac{\int_0^{\xi_s} \xi^{n+a-1}(1-\xi)^{b-1}d\xi}{\int_0^1 \xi^{n+a-1}(1-\xi)^{b-1}d\xi}] \int_0^1 \xi^{n+a-1}(1-\xi)^{b-1}d\xi$$

$$= \sum_n [d_{mn} + (c_{mn} - d_{mn}) BETAI(s, a+n, b)] BETA(a+n, b) \qquad (B9)$$

In present study, the degree of the polynomial is used as $N = 6$. Finally, the mean mixture property, $\overline{\phi}_m(x_i)$ can be calculated as

$$\overline{\phi}_m(x_i) = \frac{T}{BETA(a,b)} \qquad (B10)$$

APPENDIX C. Stoichiometric Relations For Hydrocarbon Fuels

For the hydrocarbon-air mixtures, the irreversible single-step reaction is expressed as follows:

$$C_xH_y + (x + \frac{y}{4})(O_2 + nN_2) \rightarrow xCO_2 + \frac{y}{2}H_2O + (x + \frac{y}{4})nN_2 \qquad (C1)$$

Here, n is 3.76. In the given reaction process, five species (fuel,O_2, N_2, CO_2, and H_2O) are participating the mixture composition. Once the mass fraction of fuel and oxidizer have been determined from the solutions of the transport equations, the mass fraction of the remaining species can be obtained from the following stoichimetric relations.

$$Y_{H_2O} = K_2(1 - K_1Y_{O2} - Y_{fu}) \qquad (C2)$$

$$Y_{CO_2} = K_3Y_{H_2O} \qquad (C3)$$

$$Y_{N_2} = 1 - (Y_{H_2O} + Y_{CO_2} + Y_{O_2} + Y_{fu}) \qquad (C4)$$

where

$$K_1 = 1 + n\frac{W_{N_2}}{W_{O_2}}$$

$$K_2 = \frac{\frac{y}{2}W_{H_2O}}{[\frac{y}{2}W_{H_2O} + \{(x + \frac{y}{4})nW_{n_2} + xW_{CO_2}\}]}$$

$$K_3 = \frac{xW_{CO_2}}{\frac{y}{2}W_{H_2O}}$$

APPENDIX D. Droplet Distribution Models

The present dilute spray model assumes that the fuel is injected into the combustion chamber as a fully atomized spray which consists of spherical droplets. The droplet-size distribution with the spray is represented by a finite number of size ranges. A Nukiyama-Tanasawa distribution and a Rosin-Rammler distribution are implemented in the computer code. These distributions have the following forms:

Nukiyama-Tanasawa Distribution

$$\frac{dN}{N} = A(\frac{D}{SMD})^{\alpha} e^{-B(D/SMD)^{\beta}} \frac{dD}{SMD} \qquad (D.1)$$

where dN and N are the number of computational parcels in the size range from D to $D+dD$ and the total number of computational parcels, respectively; SMD is the Sauter mean diameter; and α, β, A, and B are experimentall determined constants.

Rosin-Rammler Distribution

$$\frac{dQ}{dD} = \frac{qD^{q-1}}{X^q} e^{-(D/X)^q} \qquad (D.2)$$

$$\frac{X}{SMD} = \Gamma(1 - \frac{1}{q}) \qquad (D.3)$$

where Q is the fraction of the total volume contained in drops of diameter less than D, and X and q are constants.

SECA-TR-92-06

ADAPTION OF MULTIDIMENSIONAL GROUP PARTICLE TRACKING AND PARTICLE WALL-BOUNDARY CONDITION MODEL TO THE FDNS CODE

Subcontract 91-177
Contract No. NAS8-36955
Final Report

Prepared by:

Y. S. Chen
R. C. Farmer

Prepared for:

University of Alabama in Huntsville
Huntsville, AL 35899

March, 1992

SECA, Inc.
3313 Bob Wallace Avenue
Suite 202
Huntsville, AL 35805

Table of Contents

Introduction.....1

Governing Equation.....1

Finite Rate Chemistry Model.....3

Particulate-Phase Equations.....4

Details of the Particle Solution Method.....7

Test Cases.....10

- The Tomahawk Nozzle Flowfield.....10
- The Tomahawk Plume Flowfield.....15
- Liquid Injector Flowfields.....16

Closure.....17

Conclusions.....19

References.....20

Introduction

A particulate two-phase flow CFD model was developed based on the FDNS code (Refs. 1,2,3) which is a pressure based predictor plus multi-corrector Navier-Stokes flow solver. Turbulence models with compressibility correction (Ref.4) and the wall function models (Ref. 5) were employed as submodels. A finite-rate chemistry model (Refs. 6,7) was used for reacting flow simulation. For particulate two-phase flow simulations, a Eulerian-Lagrangian solution method using an efficient implicit particle trajectory integration scheme was developed in this study. Effects of particle-gas reaction and particle size change to agglomeration or fragmentation were not considered in this investigation.

At the onset of the present study, a two-dimensional version of FDNS which had been modified to treat Lagrangian tracking of particles (FDNS-2DEL) had already been written and was operational. The FDNS-2DEL code was too slow for practical use, mainly because it had not been written in a form amenable to vectorization on the Cray, nor was the full three-dimensional form of FDNS utilized. The specific objective of this study was to reorder the calculations into long single arrays for automatic vectorization on the Cray and to implement the full three-dimensional version of FDNS to produce the FDNS-3DEL code. Since the FDNS-2DEL code was slow, a very limited number of test cases had been run with it. This study was also intended to increase to number of cases simulated to verify and improve, as necessary, the particle tracking methodology coded in FDNS.

Governing Equation

The gas-phase governing equations of the FDNS module are the

Reynolds-averaged Navier-Stokes equations with the addition of particle drag forces and heat fluxes in the momentum equations and the energy equation, respectively. Due to the effect of large density differences between the particles and the surrounding gas, the drag force was considered to be the primary contribution to the inter-phase momentum exchange. The gas-phase governing equations are written as:

$$J^{-1}(\partial \rho q/\partial t) = \partial[-\rho U_i q + \mu_{eff} G_{ij}(\partial q/\partial \xi_j)]/\partial \xi_i + S_q$$

where q = 1, u, v, w, h, k, ϵ and α_i for the continuity, momentum, energy, turbulence model and chemical species transport equations respectively. And, the transformation parameters and effective viscosity, μ_{eff}, are given as:

$$J = \partial(\xi,\eta,\zeta)/\partial(x,y,z)$$
$$U_i = (u_j/J)(\partial \xi_i/\partial x_j)$$
$$G_{ij} = (\partial \xi_i/\partial x_k)(\partial \xi_j/\partial x_k)/J$$
$$\mu_{eff} = (\mu + \mu_t)/\sigma_q$$

The source terms in the governing equations, S_q, are given as:

$$S_q = J^{-1}\begin{bmatrix} 0 \\ -p_x + \nabla[\mu_{eff}(u_j)_x] - (2/3)(\mu_{eff}\nabla u)_x + Dx \\ -p_y + \nabla[\mu_{eff}(u_j)_y] - (2/3)(\mu_{eff}\nabla u)_y + Dy \\ -p_z + \nabla[\mu_{eff}(u_j)_z] - (2/3)(\mu_{eff}\nabla u)_z + Dz \\ Dp/Dt + h_v + H_p - u_p\,Dx - v_p\,Dy - w_p\,Dz \\ \rho(P_r - \epsilon) \\ \rho(\epsilon/k)[(C_1 + C_3 P_r/\epsilon)\,P_r - C_2\epsilon] \\ \omega_n \end{bmatrix}$$

where Dx, Dy and Dz represent the drag forces and n takes on

values between 1 and N. u_p, v_p and w_p are the particle velocity components. H_p is the rate of heat transfer per unit volume to the gas phase. h_v stands for the viscous heat flux of the gas phase. P_r stands for the turbulence kinetic energy production rate and is written as:

$$P_r = (\mu_t/\rho)[(\partial u_j/\partial x_i + \partial u_i/\partial x_j)^2/2 - 2(\partial u_k/\partial x_k)^2/3]$$

An equation of state, $\rho = p/(RT/M_w)$, is used to close the above system of equations. Turbulent Schmidt and Prandtl numbers, σ_q, for the governing equations and other turbulence model constants are given taken from Refs. 4, 6 and 7.

Finite Rate Chemistry Model

For gas-phase chemical reaction modeling, a general system of chemical reactions is written in terms of the stoichiometric coefficients (ν_{ij} and ν_{ij}') and the i-th chemical species name (M_i) of the j-th reaction as

$$\sum_i \nu_{ij} M_i = \sum_i \nu_{ij}' M_i'$$

The net rate of change in the molar concentration of species i due to reactions j , X_{ij}, is written as:

$$X_{ij} = (\nu_{ij}'-\nu_{ij}) [K_{fj}\Pi(\rho\alpha_i/M_{wi})^{\nu ij} - K_{bj}\Pi(\rho\alpha_i/M_{wi})^{\nu ij'}]$$

and the species production rate, ω_i, (in terms of mass fraction) is calculated by summing over all reactions.

$$\omega_i = M_{wi} \sum_j X_{ij}$$

where

M_{wi} = molecular weight of species i

α_i = mass fraction of species i

ρ = fluid density

K_{fj} = forward rate of reaction j

K_{bj} = backward rate of reaction j = K_{fj}/K_{ej}

K_{ej} = equilibrium constant

$= (1/RT)^{\Sigma(\nu ij'-\nu ij)} \exp(\Sigma(f_i'\nu_{ij}' - f_i\nu_{ij}))$

f_i = Gibbs free energy of species i

$K_f = A\ T^B \exp(-E/RT)$

Finally, the species continuity equations are written as:

$$\rho\ D_t\alpha_i - \nabla[(\mu_{eff}/\sigma_\alpha)\nabla\alpha_i] = \omega_i$$

where σ_α (assumed to be 0.9) represents the Schmidt number for turbulent diffusion. A penalty function is employed to ensure the basic element conservation constraints at the end of every time marching step. This is a crucial requirement for the numerical stability and accuracy of a CFD combustion model. This is accomplished by limiting the allowable changes in species concentrations, which are the solutions of the species continuity equations, for each time step such that the species mass fractions are well bounded within physical limits. The resulting limited changes are adjusted so that they are proportional to the species source terms. A similar chemistry approach and detailed turbulence submodels were reported previously (Ref. 8).

Particulate-Phase Equations

A Eulerian-Lagrangian particle tracking method was employed in FDNS to provide effects of momentum and energy exchanges between the gas phase and the particle phase. The particle

trajectories are calculated using an efficient implicit time integration method for several groups of particle sizes by which the drag forces and heat fluxes are then coupled with the gas phase equations. The equations constitute the particle trajectory and temperature history are written as:

$$DV_i/Dt = (U_i - V_i)/t_d$$
$$Dh_p/Dt = C_{pc} (T_{aw} - T_p)/t_H - 6 \sigma \epsilon f T_p^4/(\rho_p d_p)$$

where U_i = Gas Velocity
V_i = Particle Velocity
t_d = Particle Dynamic Relaxation Time
= $4 \rho_p d_p/(3 C_d \rho_c |U_i - V_i|)$
h_p = Particle Enthalpy
C_{pc} = Particle Heat Capacity
T_p = Particle Temperature
T_{aw} = Gas Recovery Temperature
t_H = Particle Thermal-Equilibrium Time
= $(\rho_p d_p)/[12 Nu \mu/(Pr d_p)]$
σ = Stefan-Boltzmann Constant
= 4.76E-13 BTU/FT^2-S-R
ϵ = Particle Emissivity = 0.20 -- 0.31
f = Radiation Interchange Factor
d_p = Particle Diameter
ρ_p = Particle Density

C_d and Nu stand for drag coefficient and Nusselt number for heat transfer which are functions of Reynolds number and relative Mach number. Typical correlations are given in Refs. 9 and 10. Carlson and Hoglund's correlation (Ref. 9) is written as:

$$C_d = (24/Re)\ (1 + 0.15\ Re^{0.687})\ (1 + e^{-a})/ [1 + M\ (3.82 + 1.28\ e^{-1.25Re/M})/Re]$$

$$Nu = (1 + 0.2295\ Re^{0.55})/ [1 + 3.42\ M\ (2 + 0.459\ Re^{0.55})/Re]$$

where $a = 0.427/M^{4.63} + 3.0/Re^{0.88}$. A more accurate but more complicated correlation for the drag coefficient is provided by Henderson (Ref. 10). That is, for Mach ≥ 1,

$$C_d = 24\ [Re + S\ \{4.33 + \exp(-0.247\ Re/S)\ (3.65 - 1.53\ T_w/T) /(1 + 0.353\ T_w/T)\}]^{-1} + \exp(-0.5*M/Re^{1/2})[0.1M^2 + 0.2M^8 + (4.5 + 0.38a) /(1 + a)] + 0.6\ S\ [1 - \exp(-M/Re)]$$

where $S = M(\gamma/2)^{1.2}$ is the molecular speed ratio. $a = 0.03\ Re + 0.48\ Re^{1/2}$. For Mach ≥ 1.75,

$$C_d = [0.9 + 0.34/M^2 + 1.86(M/Re)^{1/2}\ \{2 + 2/S^2 + 1.058\ (T_w/T)^{1/2}/S - 1/S^4\}]\ /\ [1 + 1.86\ (M/Re)^{1/2}]$$

And, for 1 < Mach < 1.75,

$$C_d = C_{d\ M=1} + (4/3)\ (M - 1)\ (C_{d\ M=1.75} - C_{d\ M=1})$$

which assumes a linear variation between M = 1 and M = 1.75.

It has been shown that the Henderson drag law gives better motor performance predictions compared with test data. The applicability and possible improvement of the Nusselt number correlation is currently being actively researched (Ref. 11).

Details of the Particle Solution Method

In the present two-phase flow model, an independent module was employed for the calculation of particle drag forces and heat flux contributions to the gas flow field. Subroutines for locating the particles and integrating their trajectories are called for each particle size group. The drag forces and heat fluxes are then saved for every grid point. These forces and fluxes are then used to evaluate the particle source terms in the gas-phase governing equations. In the present FDNS flow solver, two forms of the energy equation (i.e. static enthalpy form or total enthalpy form) can be selected. It has been found that although either form of energy equation usually gives similar solutions, the static enthalpy equation provides better definition of the liquid rocket plume shear layers, as shown by extensive solutions made for the SSME. A determination of which form the energy equation best simulates solid (two-phase) rocket motor plumes has not yet been made.

Particle wall-boundary conditions are treated by using a specified fraction of the colliding particles which stick to the wall. Particles which stick result in a decreased particle velocity normal to the wall for that particle size fraction. Therefore, for the particle size fraction which locally collides with the wall, part of the particles stick and the other part is turned more parallel to the wall. Energy exchange is assumed to be due only to the particles which stick. This model of particle wall interaction can be improved, but new experimental test data must become available in order to do so.

In the 2-D version of the FDNS flow solver, a fourth-order Runge-Kutta method was employed to integrate the particle trajectories. After a thorough test of the integration routine,

it was found that the explicit scheme can sometimes give diverged particle solutions when the source terms become large. Therefore, an implicit integration scheme was employed in the present model. For convenience, consider the X-component of the particle equation of motion. That is,

$$dX_p/dt = U_p$$
$$dU_p/dt = A\ (U_c - U_p)$$

where $A = 1/t_d$
U_c = gas velocity
U_p = particle velocity
X_p = particle location

In finite difference form the above equations can be written as:

$$X_p^{(n+1)} - X_p^{(n)} = (\Delta t/2)\ [U_p^{(n+1)} + U_p^{(n)}]$$
$$U_p^{(n+1)} - U_p^{(n)} = \Delta tA\ [U_c - U_p^{(n+1)}]$$

or

$$X_p^{(n+1)} = X_p^{(n)} + \Delta t/2\ [U_p^{(n+1)} + U_p^{(n)}]$$
$$U_p^{(n+1)} = [U_p^{(n)} + \Delta tA\ U_c]/(1+\Delta tA)$$

These two equations are unconditionally stable despite the magnitude of the source terms. To provide better time resolution, a variable time step size is chosen so that a particle would take at least 4 time steps to go across a grid cell.

The recognition that an improved integration scheme was needed for calculating the particle trajectories was a major hurdle in developing FDNS-3DEL. The explicit scheme appeared to give acceptable solutions, but detailed comparisons to previous FDNS-2DEL analyses showed that unacceptable pressure losses were

predicted. Several other factors were initially suspected of causing this solution behavior. Namely, the turbulence model, the form of the energy equation, and the particle drag law were initially suspected, and lengthy calculations were made before these effects were found not to be the cause of poor results. Since the FDNS-2DEL results were found to give good pressure field comparisons to conventional nozzle and plume flowfield codes (RAMP, SPP, and SPF-II), the Runge-Kutta method was not expected to perform poorly in the FDNS-EL code. Resolving this problem consumed much of the resources which otherwise would have been used to run a wider variety of test cases.

Test Cases

The major test case which was studied was the Tomahawk solid rocket motor nozzle analysis. Consideration of a plume flowfield and of an oxygen-hydrogen coaxial injector was also made. These cases are described in the following paragraphs.

- The Tomahawk Nozzle Flowfield

The Tomahawk nozzle flowfield was calculated with FDNS-3DEL and is shown in Figs. 1-4. This test case was chosen because comparable predictions with the FDNS-2DEL and RAMP codes had already been performed, and these other solutions were available for comparison (Ref. 12). Figures 1-4 show the velocity, Mach number, temperature, and water concentration profiles, respectively, for the chamber, nozzle, and near plume. The chamber flow was approximated to be uniform so that direct comparisons with the previous solutions could be made. The FDNS-2DEL solution predicted somewhat lower exit plane centerline gas temperatures (2250 °K) than the RAMP solution (2400 °K). The FDNS-3DEL (2470 °K) and RAMP solutions show essentially the same exit plane centerline gas temperatures. The raggedness in the temperature profile near the centerline in the nozzle appears to be due to a weak oblique shock. An apparent non-zero temperature normal gradient at the centerline in the subsonic portion of the nozzle flowfield is indicated. This is due to a very strong effect of the inlet particle flowfield boundary condition. In a complete SRM simulation which includes the burning grain, more particles would flow down the centerline from the chamber (as compared to the uniform flow case) and this subsonic temperature contour would probably change shape. The sharp breaks in the velocity, Mach number, and temperature contours locate the approximate limiting streamline of the particle laded flow with

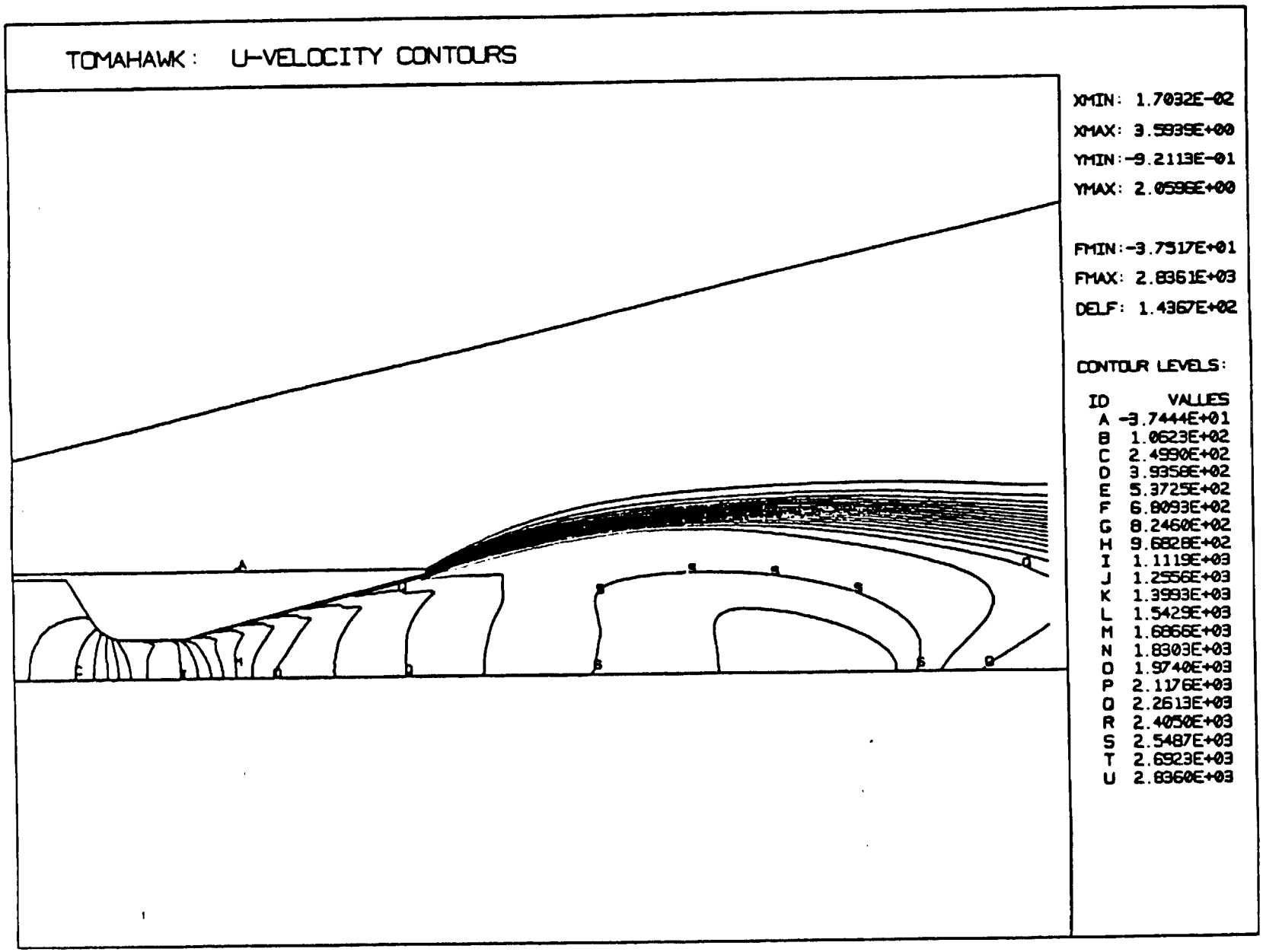
TOMAHAWK: U-VELOCITY CONTOURS
XMIN: 1.7032E-02
XMAX: 3.5939E+00
YMIN: -9.2113E-01
YMAX: 2.0598E+00
FMIN: -3.7517E+01
FMAX: 2.8361E+03
DELF: 1.4367E+02
CONTOUR LEVELS:
ID VALUES
A -3.7444E+01
B 1.0623E+02
C 2.4990E+02
D 3.9358E+02
E 5.3725E+02
F 6.8093E+02
G 8.2460E+02
H 9.6828E+02
I 1.1119E+03
J 1.2556E+03
K 1.3993E+03
L 1.5429E+03
M 1.6866E+03
N 1.8303E+03
O 1.9740E+03
P 2.1176E+03
Q 2.2613E+03
R 2.4050E+03
S 2.5487E+03
T 2.6923E+03
U 2.8360E+03

Figure 1

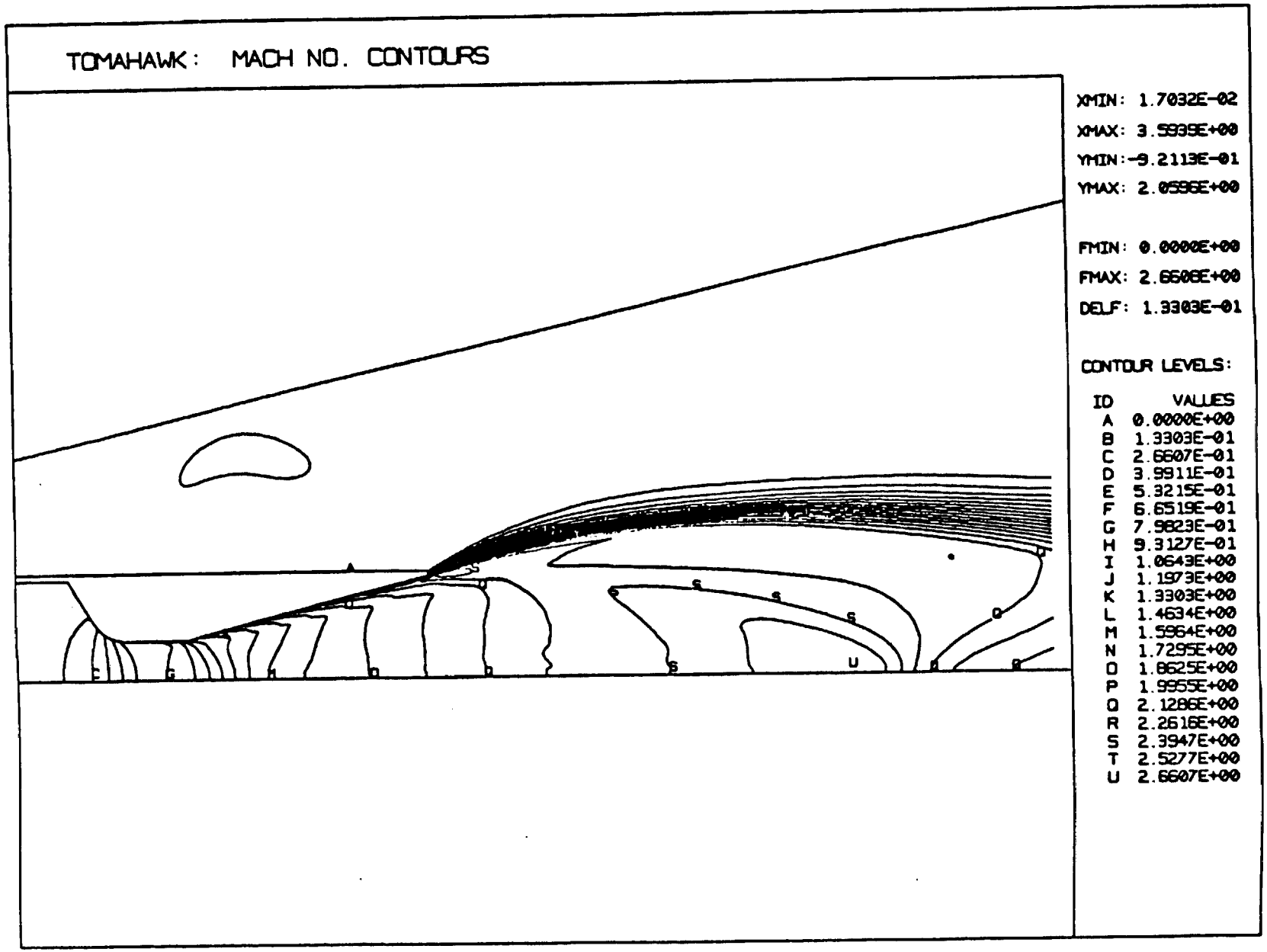
TOMAHAWK: MACH NO. CONTOURS
XMIN: 1.7032E-02
XMAX: 3.5939E+00
YMIN: -9.2113E-01
YMAX: 2.0596E+00
FMIN: 0.0000E+00
FMAX: 2.6608E+00
DELF: 1.3303E-01
CONTOUR LEVELS:
ID VALUES
A 0.0000E+00
B 1.3303E-01
C 2.6607E-01
D 3.9911E-01
E 5.3215E-01
F 6.6519E-01
G 7.9823E-01
H 9.3127E-01
I 1.0643E+00
J 1.1973E+00
K 1.3303E+00
L 1.4634E+00
M 1.5964E+00
N 1.7295E+00
O 1.8625E+00
P 1.9955E+00
Q 2.1286E+00
R 2.2616E+00
S 2.3947E+00
T 2.5277E+00
U 2.6607E+00

Figure 2

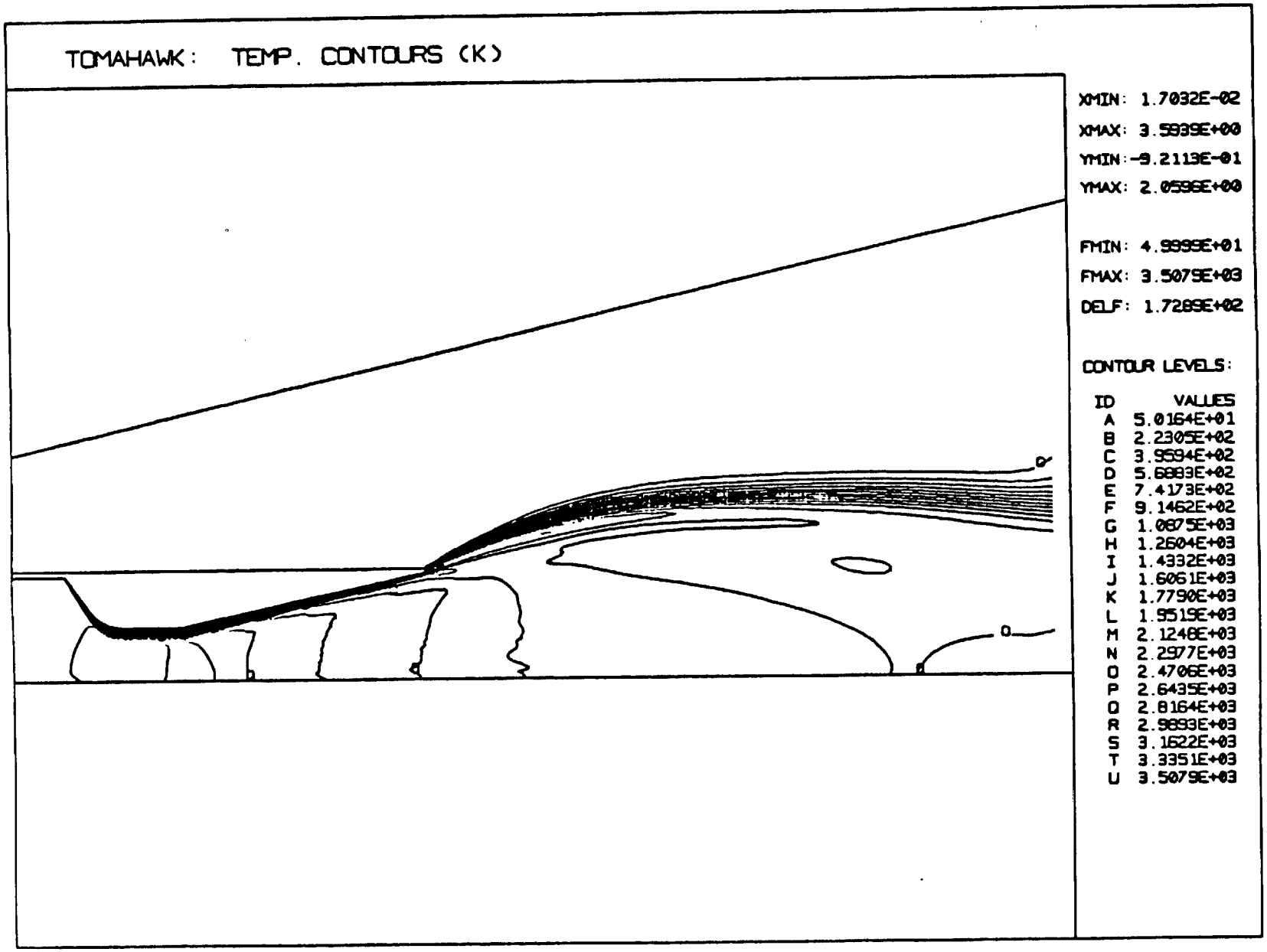
TOMAHAWK: TEMP. CONTOURS (K)
XMIN: 1.7032E-02
XMAX: 3.5939E+00
YMIN: -9.2113E-01
YMAX: 2.0596E+00
FMIN: 4.9999E+01
FMAX: 3.5079E+03
DELF: 1.7289E+02
CONTOUR LEVELS:
ID VALUES
A 5.0164E+01
B 2.2305E+02
C 3.9594E+02
D 5.6883E+02
E 7.4173E+02
F 9.1462E+02
G 1.0875E+03
H 1.2604E+03
I 1.4332E+03
J 1.6061E+03
K 1.7790E+03
L 1.9519E+03
M 2.1248E+03
N 2.2977E+03
O 2.4706E+03
P 2.6435E+03
Q 2.8164E+03
R 2.9893E+03
S 3.1622E+03
T 3.3351E+03
U 3.5079E+03

Figure 3

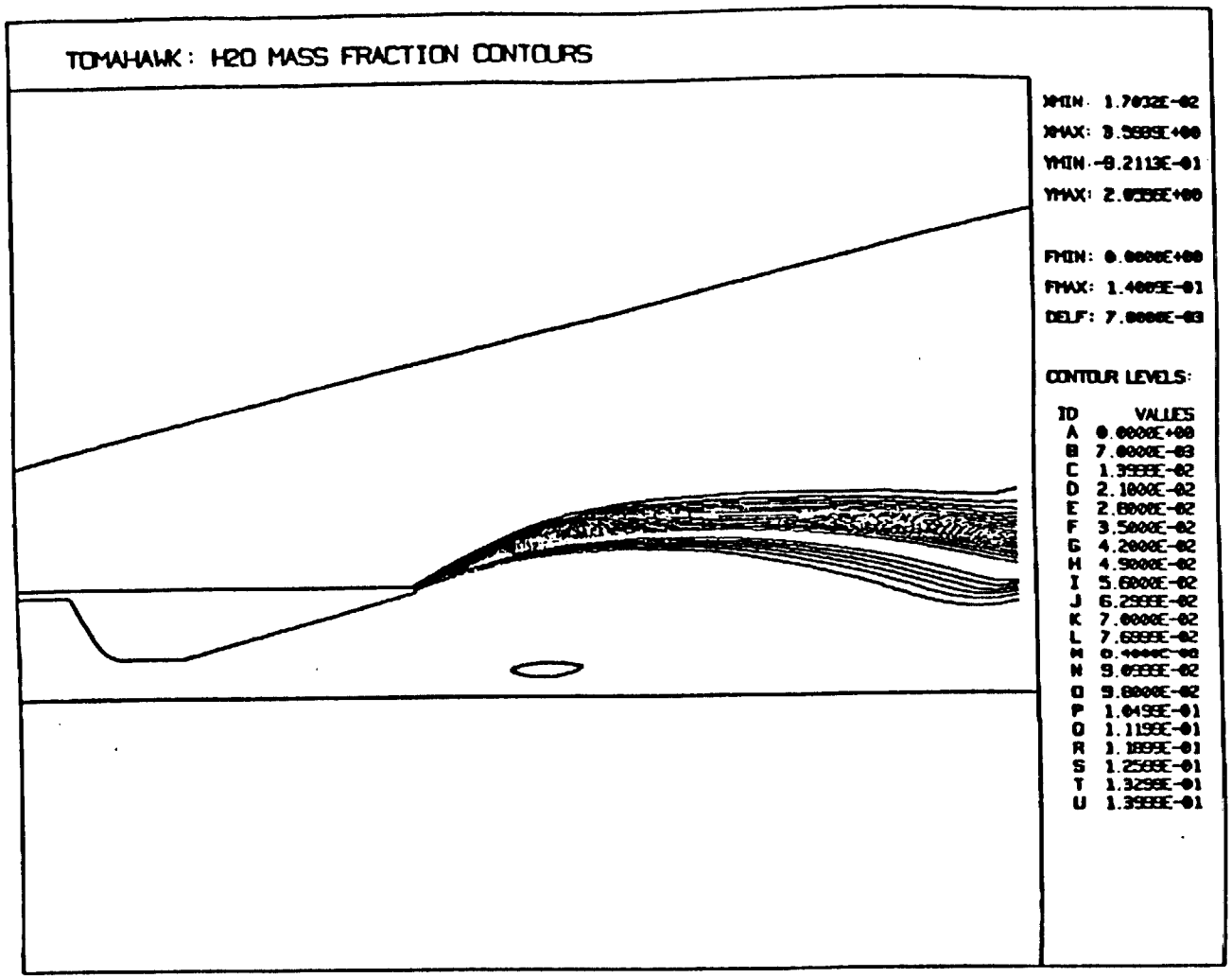
TOMAHAWK: H2O MASS FRACTION CONTOURS
XMIN: 1.7032E-02
XMAX: 3.5885E+00
YMIN: -8.2113E-01
YMAX: 2.0356E+00
FMIN: 0.0000E+00
FMAX: 1.4005E-01
DELF: 7.0000E-03
CONTOUR LEVELS:
ID VALUES
A 0.0000E+00
B 7.0000E-03
C 1.3988E-02
D 2.1000E-02
E 2.8000E-02
F 3.5000E-02
G 4.2000E-02
H 4.9000E-02
I 5.6000E-02
J 6.2988E-02
K 7.0000E-02
L 7.6988E-02
M 8.4000E-02
N 9.0988E-02
O 9.8000E-02
P 1.0498E-01
Q 1.1198E-01
R 1.1899E-01
S 1.2598E-01
T 1.3298E-01
U 1.3998E-01

Figure 4

respect to gas only flow which fills the nozzle. Both the static and total enthalpy forms of the energy equation give the same nozzle solutions. Letting the particles which hit the wall stick or elastically reflect give well behaved solutions. The only place where there is significant particle impact on the wall is at the start of the converging section. The analysis allows particles which hit the plume centerline to spectrally reflect, in order to account for particles crossing the plume centerline. However, particle drag moves the particles very parallel to the gas streamlines in the transonic region of the nozzle, such that such reflection does not occur in the case being considered.

- The Tomahawk Plume Flowfield

The near plume appears to be well predicted with FDNS-3DEL. The predicted free shear layer is sharply defined and indicates water production from afterburning reactions. Both the static and total form of the energy equation were considered. The total form of the energy equation indicates a temperature spike at the inception of the free shear layer. Better definition of the induced flow on the outside of the nozzle would probably eliminate such a spike. The static form of the energy equation does not exhibit this effect. A Mach number correction to the $k-\epsilon$ turbulence model was used for this simulation.

When the Tomahawk plume is calculated for a long distance down stream of the exit plane with FDNS-2DEL, excessively rapid plume/atmosphere mixing is predicted. This was believed to be due to the effect of crossing the Mach disc in the plume and thereby creating too much turbulent kinetic energy with the $k-\epsilon$ turbulence model being used. A similar problem exists when using the SPF/II standard JANNAF plume code (Ref. 13). The remedy in the SPF/II code is to switch turbulence models between the near

and far plumes. An insufficient number of test cases have been run with FDNS-3DEL to determine if the Mach number modified turbulence model will indeed fix this problem, although the solution is better behaved than when the extended k-ϵ turbulence model is used. This potential plume prediction problem for far-field analysis must be left for future resolution. The FDNS-3DEL code should not require any change other than turbulence model parameters to adjust the rate of plume/atmosphere mixing. It should be noted that the computed results with FDNS-2DEL, at first glance, look like the afterburning combustion reaction rates are too slow. Actually, so much of the cold atmosphere had mixed with the plume that the existence of afterburning was not apparent.

- Liquid Injector Flowfields

The current version of FDNS-3DEL does not treat mass transport from the particle phase to the gas (or continuous) phase. Also, the particle phase is treated with a lumped model such that the particle temperature is constant throughout the particle at any instant of time during the flow through the computation field. These restrictions should be removed before the code is useful for describing spray combustion. However, the spread of a droplet cloud of supercritical fuel or LOX could be described with the code without modification, if one is content with not describing local mixture ratio changes, i.e. one assumes that the supercritical lump remains a lump (or particle) in the region of the flow being analyzed. The energy transfer for supercritical injection could be easily treated in this manner because the heat of vaporization does not have to be considered. In fact, models which are based on arbitrarily supplying such heat of vaporization (Ref. 14), do not realistically describe supercritical spray phenomena. The only reason that such models

work at all is that the heat of vaporization evaluated at the temperature of the oxygen lump crudely approximates the high heat capacity of the liquid-like lump at supercritical pressures. An oxygen spray eminating from a single coaxial injector could be described with FDNS-3DEL by assuming the oxygen lump to be of a constant size and density. A demonstration calculation of this nature was considered, but the lump density would be such a very strong function of the mean lump temperature that the calculation was not performed. If accurate real-gas equation of state models were used, the stated oxygen spray simulation would be meaningful. Currently, SECA is developing the more general property evaluation for a hydrogen-oxygen engine heat transfer analysis (Ref. 15). However, the currently feasible constant property analysis was not made, because a reliable two-phase, 3-dimensional FDNS-3DEL code was not completed early enough in this study.

Closure

The calculation of two-phase reacting flows at best is a slow process. Several strategies were tried to make this process more efficient. Initially, ideal gas flow was computed, then the reactions were turned on, and finally the particle trajectories were calculated. The entire flowfield was calculated for each of these flow conditions. Recently, all of these conditions have been treated simultaneously from the beginning of the analysis. This procedure works well and results in an overall reduction in computation time. For analyzing rocket motors and their attendant plumes, it is recommended that the flowfield should be broken into subregions for analysis, in order to use the optimum step size for the Mach number range within the region. Such a restart option has been incorporated in FDNS-3DEL. For example, the motor and nozzle should be analyzed first. The computed

nozzle exit conditions should be used to calculate the near plume. The far plume should then be computed. The break between the near and far plume should be chosen somewhere between the establishment of the complex near field shock structure and the essentially balanced jet, predominately mixing dominated far field. The development of a parabolized version FDNS-3DEL to initially predict large plume structures and other large flowfields is also recommended.

Conclusions

1. A two-phase, finite-rate CFD code (FDNS-3DEL) was developed and vectorized. The Tomahawk nozzle test case indicates the CFD solution accurately simulates this flow.

2. Particle mass transfer effects are not currently included in the current code. The inclusion of these effects would be relatively simple.

3. More test cases should be run to establish the range of validity of the calculation procedure. The mechanics of the Euler-Lagrange calculation appear to be in good working order. Secondary effects, such as turbulent-mixing/shock-structure interaction require further study with more test cases. However, it should be noted that suitable experimental data to verify many of these complex flow interactions are not now available. The best one can currently do is compare CFD solutions to SPF-II type analyses.

4. Analyzing large, complex flowfields with any two-phase, finite-rate CFD code is a time consuming process, therefore utilization of all methods which would expedite such analyses should be considered. Analyzing the flowfields with carefully selected subregions and developing parabolized versions of the CFD codes are two such computational aids which should be employed.

References:

1. Y.S. Chen, AIAA Paper 88-0417, Jan. 1988.

2. Y.S. Chen, AIAA Paper 89-0286, Jan. 1989.

3. T.S. Wang and Y.S. Chen, AIAA Paper 90-2494, July 1990.

4. M.D. Sanford, AIAA Paper 91-1789, June 1991.

5. B.E. Launder and D.B. Spalding, Comp. Meth. Appli. Mech.Engr., Vol. 3, pp. 269-289, 1974.

6. Y.S. Chen and R.C. Farmer, AIAA Paper 91-1967, June 1991.

7. Y.S. Chen and R.C. Farmer, 4th Intl. symmp. CFD, Vol.1, 1991.

8. Wang, T.S., Y.S. Chen, and R.C. Farmer, "Numerical Investigation of Transient SSME Fuel Preburner Flowfield with a Pressure Based Reactive CFD Method," 7th SSME CFD Working Group Meeting, MSFC, April 1989.

9. D.J. Carlson & R.F. Hoglund, AIAA J., Vol. 2, Nov. 1964.

10. C.B. Henderson, AIAA J., Vol. 14, p. 707, June 1976.

11. Moylan, B., and P. Sulyma, "Investigation of Gas/Particle Heat Transfer Rates in Solid Rocket Motors," to be presented AIAA Nashville Meeting, June 1992.

12. Smith, S.D., Y.S. Chen, and B.L. Myruski:, "Model Development for Exhaust Plume Effects on Launch Stand Design," March 1991 Progress Report on NAS8-38472, SECA, Inc., Huntsville, AL, April 8, 1991.

13. Dash, S.M., et al, "The JANNAF Standard Plume Flowfield Code Version II (SPF-II), Volume I" Technical Report CR-RD-SS-90-4, Science Applications, Inc., Princeton, NJ, July, 1990.

14. Shuen, J.S., and V. Yang, AIAA Paper-91-0078, January 1991.

15. Freeman, J.A., R.C. Farmer and P.G. Anderson, "Heat Transfer in Rocket Engine Combustion Chambers and Regeneratively Cooled Nozzles," November, 1991 - February, 1992 Progress Report on NAS8-38961, SECA, Inc., Huntsville, AL, February, 1992.